Table 2. Sensitivity and specificity of the SD-Score algorithm

Prediction	Aberrantly spliced[a]	Normally spliced[a]
Aberrant splicing[b]	198 (24[c]/174[d])	2 (2[c]/0[d])
Normal splicing[b]	6 (1[c]/5[d])	36 (36[c]/0[d])
Total	204 (25[c]/179[d])	38 (38[c]/0[d])

The table shows the [a]actual and [b]predicted splicing consequences of [c]63 minigenes and [d]179 splicing mutations at the 5′ splice site in the literature database. The overall sensitivity of the SD-Score algorithm is 97.1% (198 of 204) and the specificity is 94.7% (36 of 38). The specificity is dependent on only our minigene results, because no report has been made, in which a mutation at the 5′ splice site has no effect on pre-mRNA splicing.

splicing *cis*-elements and possible errors in the NCBI RefSeq annotations make the SD-Score algorithm less accurate. In addition, our training dataset comprises exclusively minigenes, and minigenes are not always spliced in the same way as their endogenous counterparts (Supplementary Figure 4). Moreover, the SD-Score algorithm is not trained to predict if any of exon-skipping, activation of a cryptic site, and intron retention occurs due to a mutation. The SD-Score algorithm, however, can efficiently predict splicing consequences of our datasets with a sensitivity of 97.1% and a specificity of 94.7% (Table 2).

Comparison with the free energy, CV and R_i

Roca and colleagues (26) reported that the free energy between the 5′ splice site and U1 snRNA can be used to predict the 5′ splice site strength. The SD-Score can correctly predict 24 out of the 26 active and inactive cryptic sites in their series (data not shown). The Pearson's correlation coefficient between the SD-Score and the free energy in their series was 0.792, implying that these two parameters are likely mutually dependent.

We used our training dataset of 31 minigenes and validation dataset of 32 additional minigenes in an attempt to develop similar algorithms for the CV (21) and the R_i (7,8). We found that either the CV or R_i alone is not as efficient as the SD-Score algorithm for predicting splicing mutations (Figure 4). Both the CVs and R_is are based on the sum of information of each position in a sequence. On the other hand, the SD-Score represents information of the entire sequence of the 5′ splice site, which should include mutual interdependence between multiple positions. The SD-Score, CV and R_i, however, are mutually complementary, and our algorithm indeed achieved a high sensitivity and a high specificity with the help of ΔR_i values.

We also attempted to create a similar algorithm for the 3′ splice site but were unsuccessful, likely because the 3′ splice site includes at least three splicing *cis*-elements, and because a limited number of splicing mutations have been identified at the 3′ splice site.

Underestimated exonic splicing mutations

Most exonic splicing mutations affecting the 5′ splice site have been reported at position −1. On the other hand, to our knowledge, only 2 and 14 exonic splicing mutations have been reported at position −3 and −2, respectively (Supplementary Tables 2 and 3). When we introduced *in silico* all possible mutations that substitute an NCp-nuc for a Cp-nuc at positions −3, −2 and −1 into the 189 249 5′ splice sites in the human genome, the SD-Score algorithm predicted that 37.8%, 88.8% and 96.8% of these mutations would affect pre-mRNA splicings, respectively (Table 3). These percentages, as well as those of

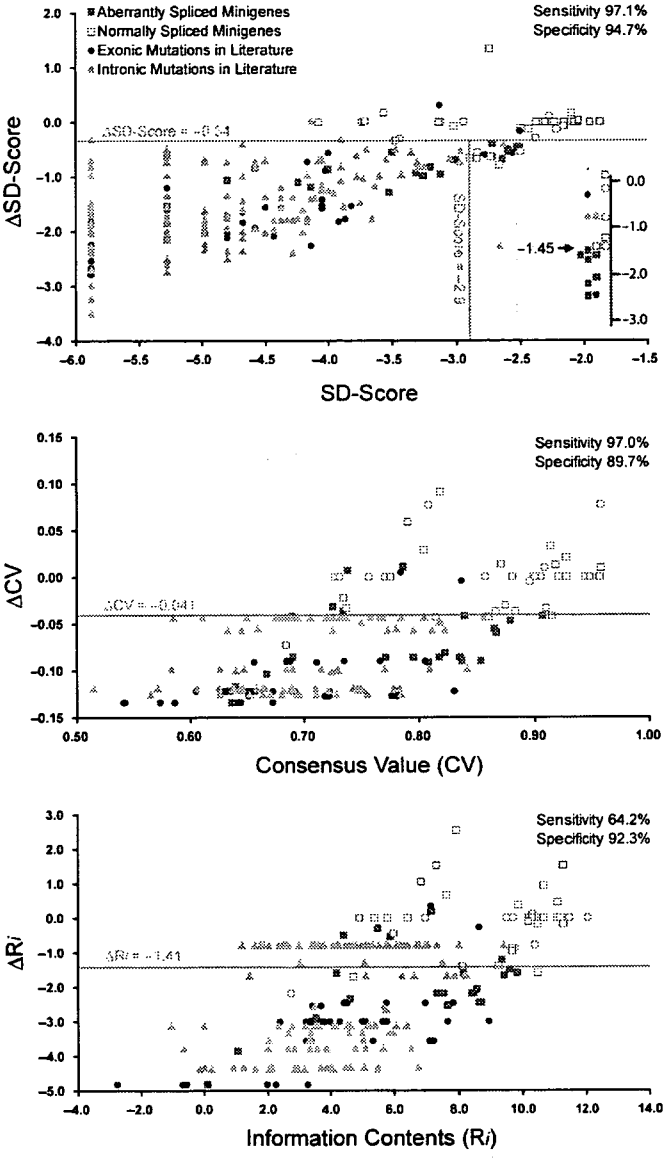

Figure 4. Scatter graphs of the SD-Scores (**A**), the CVs (**B**) and the R_is (**C**) of 63 minigenes and 179 splicing mutations in the literature database. Thirty-nine normally spliced and 24 aberrantly spliced minigenes and 37 exonic and 142 intronic splicing mutations are plotted on each graph. Thresholds for the CVs and R_is were determined with the JMP-IN statistical software to give the best discrimination between normal and aberrant splicings. For the SD-Score, we used 31 minigenes as a training data set and other 32 minigenes as a validation data set. We obtained the similar thresholds of the SD-Score, even when we included 63 minigenes in our training data set (data not shown).

Table 3. Predicted ratios of exonic and intronic splicing mutations

Position	−3	−2	−1	+1	+2	+3	+4	+5	+6
Complementary nucleotide	C	A	G	G	T	A	A	G	T
A	1.8	–	93.7	–	–	–	–	93.9	56.9
C	–	89.6	99.7	–	–	99.9	94.4	98.6	75.4
G	35.0	90.5	–	–	–	48.7	96.2	–	56.7
T	76.7	86.2	97.1	–	–	99.9	94.3	97.0	–
All mutations	37.8	88.8	96.8	–	–	82.8	95.0	96.5	63.0

Numbers indicate the percentages of generating splicing mutations according to the SD-Score algorithm. The mutations are weighed by the number of occurrences of the native 5′ splice site. For example, the CAG|GTGAGG sequence, which is observed at 2562 splice sites in the human genome, has a SD-Score of −1.868. A C-to-T mutation at position −3 should generate TAG|GTGAGG, which is observed at 145 splice sites and has a SD-Score of −3.116. The ΔSD-Score of the mutation is thus −1.247. This mutation is predicted to cause aberrant splicing and is counted as 2562 mutations instead of one, because the chance that this mutation occurs should be higher than those of rare 5′ splice sites. Only mutations that substitute an NCp-nuc for a Cp-nuc are considered in this analysis, and 2466918 mutations have been simulated.

intronic mutations at the 5′ splice site, are much higher than we expected. We hope that the SD-Score algorithm serves as a practical tool to predict splicing mutations at the 5′ splice site and sheds light on underestimated aberrant splicings in human diseases.

SUPPLEMENTARY DATA

Supplementary Data are available at NAR online. Supplementary Table 5 is an Excel program to calculate the SD-Score algorithm.

ACKNOWLEDGEMENTS

We acknowledge Dr Kazunori Imaizumi, University of Miyazaki, Miyazaki, Japan and Dr Alan M. Weiner, University of Washington, Seattle, WA, USA for providing us with experimental materials and Dr Masao Okazaki, Jikei University, Tokyo, Japan for preparing publication materials. This work was supported by Grants-in-Aid for Scientific Research (B) and Scientific Research on Priority Areas from the Ministry of Education, Culture, Sports, Science, and Technology of Japan, and by Research Grant for Nervous and Mental Disorders from the Ministry of Health, Labor, and Welfare of Japan, and was also supported in part by grants from the Naito Foundation and the Takeda Science Foundation. Funding to pay the Open Access publication charges for this article was provided by Grants-in-Aid for the Scientific Research on Priority Areas "System Genomics" from the Ministry of Education, Culture, Sports, Science, and Technology of Japan.

Conflict of interest statement. None declared.

REFERENCES

1. Reed,R. (2000) Mechanisms of fidelity in pre-mRNA splicing. *Curr. Opin. Cell Biol.*, **12**, 340–345.
2. Zhang,M.Q. (1998) Statistical features of human exons and their flanking regions. *Hum. Mol. Genet.*, **7**, 919–932.
3. Black,D.L. (2003) Mechanisms of alternative pre-messenger RNA splicing. *Annu. Rev. Biochem.*, **72**, 291–336.
4. Lesser,C.F. and Guthrie,C. (1993) Mutations in U6 snRNA that alter splice site specificity: implications for the active site. *Science*, **262**, 1982–1988.
5. Kandels-Lewis,S. and Seraphin,B. (1993) Involvement of U6 snRNA in 5′ splice site selection. *Science*, **262**, 2035–2039.
6. Kim,C.H. and Abelson,J. (1996) Site-specific crosslinks of yeast U6 snRNA to the pre-mRNA near the 5′ splice site. *RNA*, **2**, 995–1010.
7. Rogan,P.K. and Schneider,T.D. (1995) Using information content and base frequencies to distinguish mutations from genetic polymorphisms in splice junction recognition sites. *Hum. Mutat.*, **6**, 74–76.
8. Rogan,P.K., Faux,B.M. and Schneider,T.D. (1998) Information analysis of human splice site mutations. *Hum. Mutat.*, **12**, 153–171.
9. Ohno,K., Anlar,B., Özdirim,E., Brengman,J.M., DeBleecker,J.L. and Engel,A.G. (1998) Myasthenic syndromes in Turkish kinships due to mutations in the acetylcholine receptor. *Ann. Neurol.*, **44**, 234–241.
10. Ohno,K., Milone,M., Shen,X.M. and Engel,A.G. (2003) A frame-shifting mutation in *CHRNE* unmasks skipping of the preceding exon. *Hum. Mol. Genet.*, **12**, 3055–3066.
11. Burge,C.B., Padgett,R.A. and Sharp,P.A. (1998) Evolutionary fates and origins of U12-type introns. *Mol. Cell*, **2**, 773–785.
12. Levine,A. and Durbin,R. (2001) A computational scan for U12-dependent introns in the human genome sequence. *Nucleic Acids Res*, **29**, 4006–4013.
13. Alioto,T.S. (2007) U12DB: a database of orthologous U12-type spliceosomal introns. *Nucleic Acids Res.*, **35**, D110–115.
14. Sheth,N., Roca,X., Hastings,M.L., Roeder,T., Krainer,A.R. and Sachidanandam,R. (2006) Comprehensive splice-site analysis using comparative genomics. *Nucleic Acids Res.*, **34**, 3955–3967.
15. Stenson,P.D., Ball,E.V., Mort,M., Phillips,A.D., Shiel,J.A., Thomas,N.S., Abeysinghe,S., Krawczak,M. and Cooper,D.N. (2003) Human Gene Mutation Database (HGMD): 2003 update. *Hum. Mutat.*, **21**, 577–581.
16. Hatano,Y., Li,Y., Sato,K., Asakawa,S., Yamamura,Y., Tomiyama,H., Yoshino,H., Asahina,M., Kobayashi,S. *et al.* (2004) Novel *PINK1* mutations in early-onset parkinsonism. *Ann. Neurol.*, **56**, 424–427.
17. Hering,R., Strauss,K.M., Tao,X., Bauer,A., Woitalla,D., Mietz,E.M., Petrovic,S., Bauer,P., Schaible,W. *et al.* (2004) Novel homozygous p.E64D mutation in *DJ1* in early onset Parkinson disease (PARK7). *Hum. Mutat.*, **24**, 321–329.
18. Chen,W., Kubota,S., Ujike,H., Ishihara,T. and Seyama,Y. (1998) A novel Arg362Ser mutation in the sterol 27-hydroxylase gene (*CYP27*): its effects on pre-mRNA splicing and enzyme activity. *Biochemistry (Mosc).* **37**, 15050–15056.
19. Carmel,I., Tal,S., Vig,I. and Ast,G. (2004) Comparative analysis detects dependencies among the 5′ splice-site positions. *RNA*, **10**, 828–840.
20. Kammler,S., Leurs,C., Freund,M., Krummheuer,J., Seidel,K., Tange,T.O., Lund,M.K., Kjems,J., Scheid,A. *et al.* (2001) The sequence complementarity between HIV-1 5′ splice site SD4 and U1 snRNA determines the steady-state level of an unstable env pre-mRNA. *RNA*, **7**, 421–434.
21. Shapiro,M.B. and Senapathy,P. (1987) RNA splice junctions of different classes of eukaryotes: sequence statistics and functional implications in gene expression. *Nucleic Acids Res.*, **15**, 7155–7174.
22. Williamson,D., Brown,K.P., Langdown,J.V. and Baglin,T.P. (1995) Haemoglobin Dhofar is linked to the codon 29 C–>T (IVS-1 nt-3) splice mutation which causes beta+ thalassaemia. *Br. J. Haematol.*, **90**, 229–231.
23. Ries,S., Aslanidis,C., Fehringer,P., Carel,J.C., Gendrel,D. and Schmitz,G. (1996) A new mutation in the gene for lysosomal acid

lipase leads to Wolman disease in an African kindred. *J. Lipid Res.*, **37**, 1761–1765.
24. Slaugenhaupt,S.A., Mull,J., Leyne,M., Cuajungco,M.P., Gill,S.P., Hims,M.M., Quintero,F., Axelrod,F.B. and Gusella,J.F. (2004) Rescue of a human mRNA splicing defect by the plant cytokinin kinetin. *Hum. Mol. Genet.*, **13**, 429–436.
25. Brichta,L., Holker,I., Haug,K., Klockgether,T. and Wirth,B. (2006) In vivo activation of SMN in spinal muscular atrophy carriers and patients treated with valproate. *Ann. Neurol.*, **59**, 970–975.
26. Roca,X., Sachidanandam,R. and Krainer,A.R. (2005) Determinants of the inherent strength of human 5′ splice sites. *RNA*, **11**, 683–698.

Published online 20 September 2007

Nucleic Acids Research, 2007, Vol. 35, No. 18 ***e123***
doi:10.1093/nar/gkm699

Thermodynamic instability of siRNA duplex is a prerequisite for dependable prediction of siRNA activities

Masatoshi Ichihara[1,2], Yoshiki Murakumo[2], Akio Masuda[3], Toru Matsuura[3], Naoya Asai[2], Mayumi Jijiwa[2], Maki Ishida[2], Jun Shinmi[3], Hiroshi Yatsuya[4], Shanlou Qiao[1], Masahide Takahashi[2,5] and Kinji Ohno[3,*]

[1]Department of Biomedical Sciences, College of Life and Health Sciences, Chubu University, 1200 Matsumoto, Kasugai 487-8501, [2]Department of Pathology, [3]Division of Neurogenetics and Bioinformatics, Center for Neurological Diseases and Cancer, [4]Department of Public Health/Health Information Dynamics, Field of Social Life Science, Program in Health and Community Medicine and [5]Division of Molecular Pathology, Center for Neurological Diseases and Cancer, Nagoya University Graduate School of Medicine, 65 Tsurumai, Showa-ku, Nagoya 466-8550, Japan

Received July 27, 2007; Revised and Accepted August 22, 2007

ABSTRACT

We developed a simple algorithm, *i-Score* (inhibitory-Score), to predict active siRNAs by applying a linear regression model to 2431 siRNAs. Our algorithm is exclusively comprised of nucleotide (nt) preferences at each position, and no other parameters are taken into account. Using a validation dataset comprised of 419 siRNAs, we found that the prediction accuracy of *i-Score* is as good as those of *s-Biopredsi*, *ThermoComposition21* and *DSIR*, which employ a neural network model or more parameters in a linear regression model. *Reynolds* and *Katoh* also predict active siRNAs efficiently, but the numbers of siRNAs predicted to be active are less than one-eighth of that of *i-Score*. We additionally found that exclusion of thermostable siRNAs, whose whole stacking energy (ΔG) is less than -34.6 kcal/mol, improves the prediction accuracy in *i-Score*, *s-Biopredsi*, *ThermoComposition21* and *DSIR*. We also developed a universal target vector, pSELL, with which we can assay an siRNA activity of any sequence in either the sense or antisense direction. We assayed 86 siRNAs in HEK293 cells using pSELL, and validated applicability of *i-Score* and the whole ΔG value in designing siRNAs.

INTRODUCTION

When we study the molecule of our interest, we up- and down-regulate its expression either in cells or in bodies, and analyze their effects by morphological, physiological and biochemical modalities. Recently, RNA interference (RNAi) has emerged as a simple and robust method to specifically silence a gene expression (1–3). In mammals, 21- to 27-nucleotide (nt) double-stranded RNA or small interfering RNA (siRNA), which is specific to a gene of our interest, is introduced into cells to induce RNAi (4,5).

To achieve efficient and specific gene silencing by siRNA in mammals, an accurate siRNA-designing algorithm is crucial. Numerous algorithms have been reported to date. The algorithm can be arbitrarily divided into two categories: the first-generation algorithms that are based on a small number of observations and the second-generation algorithms that arise from a large number of observations. The first-generation algorithms exploit a variety of siRNA features such as the thermodynamic stability (6,7), base preferences at specific positions (8–12), mRNA secondary structures (13–16) and uniqueness of the target site (17,18). These siRNA features are also summarized in review articles (19–21). The first-generation algorithms disclosed the fundamental requirements for designing active siRNAs.

The prediction accuracies of the first-generation algorithms, however, were not high enough to our satisfaction (22). To improve the prediction accuracy, Huesken and colleagues (23) developed a new algorithm, *Biopredsi*, by applying an artificial neural network model to 2431 siRNAs. *Biopredsi* achieved a high correlation coefficient of 0.66 between the observed and predicted siRNA activities. The artificial neural network modeling, on which *Biopredsi* depends, however, is 'black box' in itself, and there is no sense in making further inspections of each parameter.

*To whom correspondence should be addressed. Tel: +81 52 744 2446; Fax: +81 52 744 2449; Email: ohnok@med.nagoya-u.ac.jp

In the past two years, the second-generation algorithms emerged by analyzing the Huesken's dataset (24–29). Most algorithms, however, employ complicated mathematical models and depend on calculations that cannot be readily traced, which also prevent us from evaluating these algorithms. Matveeva and colleagues (29) recently compared nine siRNA-designing tools, and concluded that *Biopredsi*, as well as *ThermoComposition* by Shabalina *et al.* (24) and *DSIR* by Vert *et al.* (27), are the best predictors of active siRNAs. The *ThermoComposition* and *DSIR* algorithms employ a linear regression model, which directly indicates nucleotide preferences at each position.

We developed here a simple siRNA prediction algorithm, *i-Score* (inhibitory-Score), based on a linear regression model. The *i-Score* algorithm can predict active siRNAs to the similar extents as *Biopredsi*, *ThermoComposition* and *DSIR*, and is better than the six first-generation algorithms. The *i-Score* algorithm is exclusively composed of the nucleotide preference scores, and is more straightforward than any of the second-generation algorithms. We also found that the whole ΔG value, which represents the stability of the siRNA duplex, ensures accurate prediction of siRNA activities in the four second-generation algorithms, and improves a correlation coefficient to more than 0.7. Additionally, we developed a new validation vector, pSELL, to assay an siRNA activity of any sequence in either the sense or antisense direction simply by synthesizing a pair of oligonucleotides. The synthesized oligonucleotides are inserted into both the pSELL validation vector and the pDual effector vector (30). We validated the efficacy of *i-Score*, as well as the thermostability threshold, by analyzing 86 siRNAs in HEK293 cells.

MATERIALS AND METHODS

Datasets

Dataset A is comprised of 2431 siRNAs reported by Huesken and colleagues (23). The quality of this dataset is ensured by the Gaussian distribution of their potencies. Dataset A is randomly divided into 1600 and 831 siRNAs (Supplementary Table 3). We made five pairs of subsets from dataset A. After confirming that all five pairs gave rise to similar results, we chose a pair of subsets A1600 and A831 without any bias. Dataset B is comprised of 419 siRNAs reported in five other articles (6,8,9,31,32). Each report shows a small number of siRNAs, and the quality of their datasets is variable from report to report.

Training and validation of prediction algorithms

For both modeling and validation analyses, we employed the 'standard least square fitting' functionality of the JMP-IN statistical software Ver. 5.1.1 (SAS Institute, Cary, NC) with its default settings. *i-Score* and *i-Score1600* are trained using dataset A and subset A1600, respectively. As the actual parameters of *Biopredsi* are not published anywhere, we developed a similar scoring system, *s-Biopredsi* for simulated *Biopredsi*, by applying a single-node neural network model on 2182 siRNAs in subset A (Supplementary Table 3), which is identical to those employed to develop *Biopredsi* (23). We again employed the 'neural network modeling' functionality of the JMP-IN software. We found a high correlation coefficient ($R = 1.0000$) between *Biopredsi* and *s-Biopredsi* with the remaining 249 siRNAs in dataset A. We also obtained a total of 400 *Biopredsi* scores from two independent genes with the *Biopredsi* web server (http://www.biopredsi.org/), and compared them to our *s-Biopredsi* scores. Correlation coefficients between *Biopredsi* and *s-Biopredsi* were 0.9999 and 0.9995 for these two genes. Hence *s-Biopredsi* is similar to *Biopredsi*. *s-Biopredsi1600* also employs a single-node neural network modeling, but is trained using subset A1600, so that subset A831 can be used for the validation analysis.

For the receiver operating characteristic (ROC) analysis, we employed the 'logistic regression' functionality of the JMP-IN software, as well as the 'ROC curve' functionality of the SPSS 15.0.1 software (SAS Institute, Cary, NC).

We developed *i-Score* designer (Supplementary Data) with Excel VBA on Windows. We implemented 11 algorithms including *i-Score* by simulating published algorithms and parameters, and confirmed that the *i-Score* designer gives the same scores as those reported by each article. *s-Biopredsi* is similar to, but different from, *Biopredsi* as indicated above. For *ThermoComposition19* and *ThermoComposition21*, the *i-Score* designer calls executable files that have been developed by Matveeva and colleagues (29).

Construction of pSELL and pDual vectors

To validate the prediction accuracy of *i-Score*, we developed a universal target vector, pSELL, which can accommodate any target sequences (Figure 5A). We first excised EGFP from pIRES2-EGFP (Clontech, Mountain View, CA, USA) and placed it upstream of IRES. We then inserted the firefly luciferase gene downstream of IRES, and made pCMV-EGFP-IRES-Luc. We additionally inserted a part of the LacZ gene between the target-cloning site and IRES so that IRES-binding proteins do not mask the upstream target sequence. We next substituted the SV40 promoter for the CMV promoter, and made pSV40-EGFP-LacZ-IRES-Luc (pSELL). We mutated an extra HindIII restriction site within IRES, and exploited the BglII, HindIII and BamHI restriction sites between EGFP and IRES to accommodate a target sequence in either the sense or antisense direction.

We also constructed an siRNA-generating vector, pDual, according to Zheng and colleagues (30). Briefly, we inserted the mouse U6 promoter and the human H1 promoter in opposite directions in pBluescript SK(-) (Stratagene, La Jolla, CA, USA). We also introduced a BglII site so that the siRNA sequence can be inserted between the HindIII and BglII sites flanked by the U6 and H1 promoters.

Cell culture and transfection

Human embryonic kidney (HEK) 293 cells were maintained in Dulbecco's modified Eagle's medium (DMEM) supplemented with 10% fetal bovine serum. In all assays, 1.5×10^5 HEK293 cells were plated on 24-well dishes 12 h before transfection. Cells were subsequently transfected with 0.3 μg of the pDual effector vector, 0.03 μg of the pSELL target vector and 0.03 μg of phRL-TK encoding the Renilla luciferase (Promega, Madison, WI, USA) using the FuGENE6 Transfection Reagent (Roche Applied Science, Basel, Switzerland). After incubation for 3 days, firefly and Renilla luciferase activities were measured using the Dual-Luciferase Reporter Assay System (Promega). Silencing activity (% inhibition) of each siRNA is calculated by dividing the relative luciferase activity in the presence of the pDual target vector by the relative luciferase activity in the presence of a control pDual vector lacking an insert.

RESULTS

Development of a simple algorithm, *i-Score*, for prediction of siRNA activities

In order to develop a simple algorithm to predict active siRNAs, we collated two datasets (Supplementary Table 3). We applied a linear regression model to dataset A comprised of 2431 siRNAs to construct a prediction algorithm, *i-Score* for inhibitory score, and validated it with dataset B comprised of 419 siRNAs. Although dataset A is comprised of 21-nt siRNA sequences, we eliminated 2-nt overhangs at the 3′ end of the antisense strand and employed 19 nt that make an siRNA duplex, in order to validate our algorithm with dataset B, which is comprised of 19-nt sequences. Our preliminary analysis using subsets A1600 and A831 demonstrated that 19-nt analysis is as good as 21-nt analysis in our linear regression model (data not shown).

Our linear regression model determines nucleotide preferences at each position of siRNA, which is then used as scoring parameters to calculate *i-Score* (Figure 1A). We normalized the scoring parameters to give the best and worst *i-Scores* of 100 and 0, respectively (Figure 1B and Supplementary Table 1). The scoring parameters directly demonstrate which nucleotides are preferred at which positions. Previous reports address the importance of G/C at positions 18 and 19 on the antisense strand, as well as a stretch of A/T at the 5′ end on the antisense strand (6,7). Our results also conform to this notion. In addition, highly positive and negative scoring parameters in our analysis are located at previously reported preferred and unfavorable nucleotides, respectively (6,23,24,27).

Comparison of *i-Score* with three other second-generation algorithms of *s-Biopredsi*, *Thermocomposition21* and *DSIR*

To test how efficiently *i-Score* predicts siRNA activities, we plotted 419 siRNA activities in dataset B against *i-Scores* (Figure 2A). We similarly plotted the observed

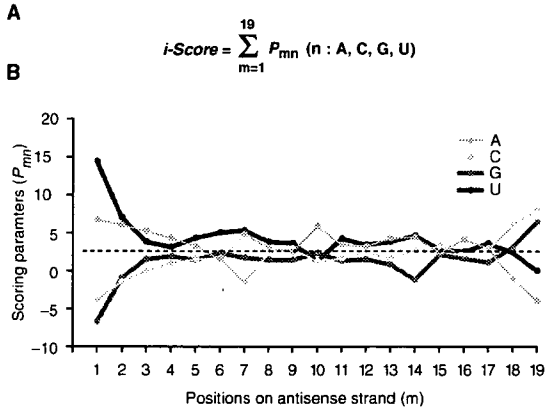

Figure 1. Definition of *i-Score* (**A**) and scoring parameters at each position (**B**). Parameters are normalized to give the best and the worst *i-Scores* of 100 and 0, respectively. The average score at each position is 2.60 (dotted line). Scores above 2.60 indicate preferred nucleotides. '*P*' is a probability score of nucleotide '*n*' at position '*m*' on the antisense strand (Supplementary Table 1).

and predicted siRNA activities with *s-Biopredsi*, *Thermocomposition21* and *DSIR* (Figure 2B–D). None of these algorithms employs dataset B in the process of training parameters. The correlation coefficients indicate that *i-Score* is as good as the three other second-generation algorithms (Table 1). For all the algorithms, the correlation coefficients with dataset A are superior to those with dataset B, implying possible overfitting with the training dataset A.

The ROC curve is a plot of sensitivity versus 1-specificity, and is widely applied to compare efficiencies of different algorithms in a variety of biomedical fields. The ROC analysis with dataset B also demonstrates that the prediction accuracies of the four algorithms are not statistically different (Figure 2E).

We also examined the correlation coefficients among *i-Score*, *s-Biopredsi*, *ThermoComposition21* and *DSIR*, and found that *i-Score*, *s-Biopredsi* and *DSIR* are close to each other, whereas *ThermoComposition21* is unique compared to the other three algorithms (Supplementary Table 2).

Comparison of the first- and second-generation algorithms

We next compared *i-Score* with *s-Biopredsi*, as well as with six other first-generation algorithms of *Reynolds*, *Ui-Tei*, *Amarzguioui*, *Katoh*, *Hsieh* and *Takasaki*, using subset A831 (Supplementary Figure 1 and Table 2). Both *i-Score* and *s-Biopredsi* are classified into the second-generation algorithms, because these are based on dataset A. As subset A831 is included in the training dataset A for *i-Score* and *s-Biopredsi*, we employed *i-Score1600* and *s-Biopredsi1600*, which we trained with subset A1600, in order to strictly avoid overfitting.

When we sort siRNAs in descending order of predicted scores and choose siRNAs above a given threshold, the ratio of active siRNAs among the selected siRNAs is inversely correlated with the number of selected siRNAs for all the algorithms (Table 2). Namely, if an algorithm chooses more siRNAs, the chance of obtaining active

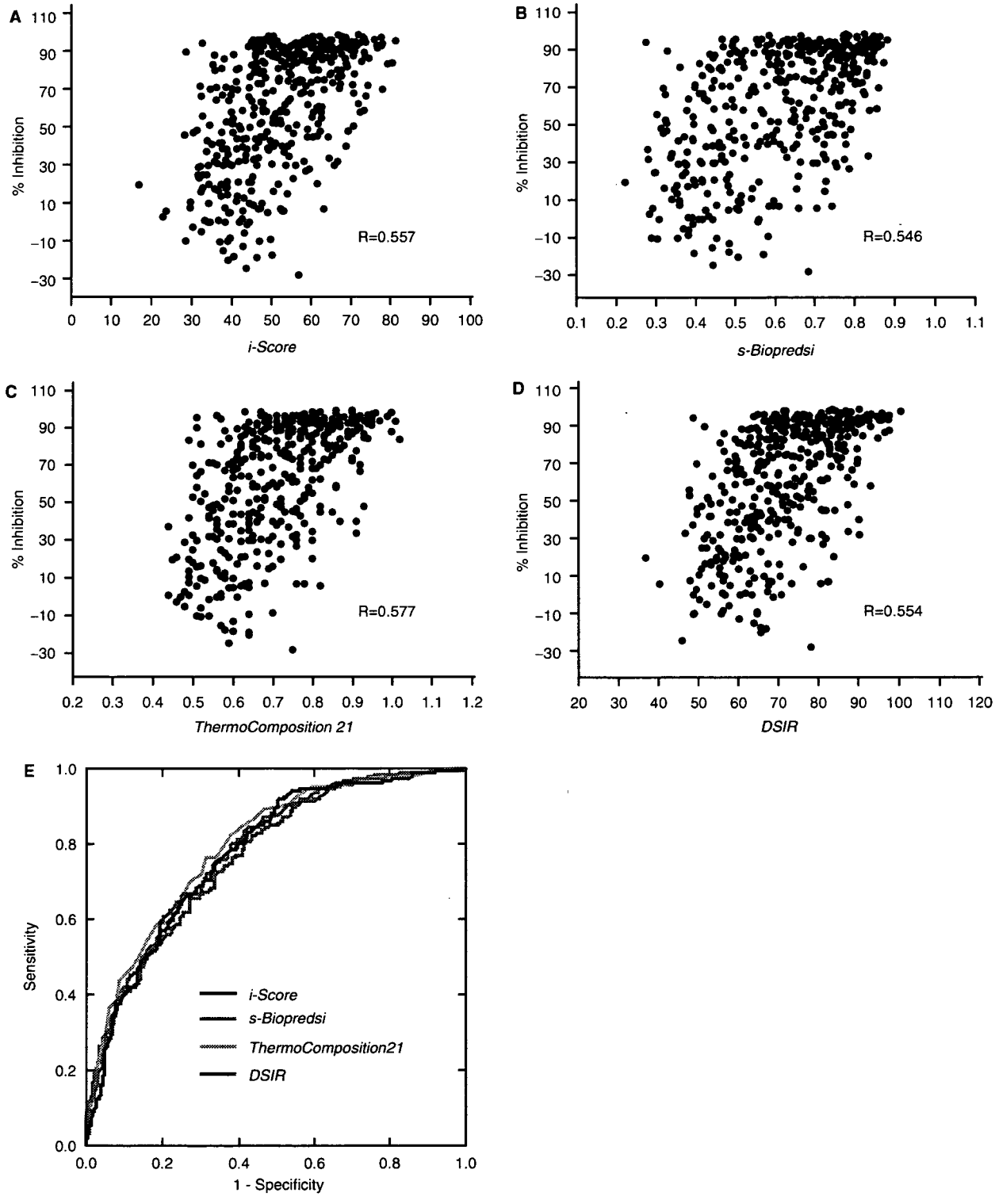

Figure 2. Observed siRNA activities in dataset B are plotted against predicted siRNA activities by *i-Score* (**A**), *s-Biopredsi* (**B**), *ThermoComposition21* (**C**) and *DSIR* (**D**). '*R*' values represent the Pearson correlation coefficients, which are also indicated in Table 1. (**E**) ROC curves of the four algorithms. Areas under the curves (AUC) of *i-Score*, *s-Biopredsi*, *ThermoComposition21* and *DSIR* are 0.776 (95% confidence interval, 0.732–0.820), 0.770 (0.726–0.814), 0.795 (0.753–0.837) and 0.781 (0.738–0.825), respectively. There are no statistical differences of AUCs among the four algorithms.

siRNAs becomes less. siRNAs with *i-Score1600* $\geq$ 65.9 constitute 8.8% of subset A831, and 90% of the siRNAs in this category are active. Similarly, siRNAs with *s-Biopredsi1600* $\geq$ 0.807 comprise 8.8% of subset A831, and 90% are active. In the current analysis, *Reynolds* and *Katoh* reach a ~90% success rate, whereas *Ui-Tei*, *Amarzguioui*, *Hsieh* and *Takasaki* do not (Table 2). siRNAs with *Reynolds* $\geq$ 9 constitute 1.1% of subset

Table 1. Pearson correlation coefficients between observed and predicted siRNA activities by four second-generation algorithms

	Dataset A	Dataset B
i-Score	0.635	0.557
s-Biopredsi	0.665	0.546
ThermoComposition21	0.635	0.577
DSIR	0.687	0.554

Dataset A is used to train all the algorithms, whereas dataset B is not used as a training dataset in any algorithms.

A831, and 88.9% are active. Similarly, siRNAs with *Katoh* > 101.1 comprise 0.7% of subset A831, and 90% are active. Therefore, when we design siRNAs expecting a ~90% success rate, *i-Score1600* and *s-Biopredsi1600* would be able to predict at least eight times more numbers of siRNAs compared to *Reynolds* and *Katoh*. This likely represents the most beneficial advantage of the second-generation algorithms over the first-generation ones.

Whole ΔG value, as an indicator of thermostability of siRNA duplex, is a key determinant of accurate prediction

We next sought for another parameter that potentially improves the correlation coefficient between the observed and predicted siRNAs with *i-Score*. In the scattered plot of the observed and predicted siRNA activities, we observe a subgroup of effective siRNAs in which *i-Scores* are falsely low (area L in Figure 3A and B). As siRNAs in area L make the correlation coefficient low, we searched for a shared feature among siRNAs in area L. For this purpose, we calculated 12 parameters for each siRNA: stacking energy (ΔG) of the secondary structure of siRNA (38), maximum GC stretch within siRNA,%GC contents spanning the antisense positions 1–19, 3–7 and 1–17, and stacking energies (ΔG) spanning the antisense positions 1–19, 3–17, 11–19, 1–9, 11–17, 3–9, 1–5 and 1–17. We divided the 419 siRNAs in dataset B into two subsets by gradually changing the threshold for each parameter, and analyzed the correlation coefficients between the two subsets.

This analysis revealed that siRNAs with a stable stacking energy at positions 1–19 (the whole ΔG value) tend to give rise to a low correlation coefficient. A contour plot of the whole ΔG values also illustrates that siRNAs in area L have stable stacking energies of ≤ -37 kcal/mol (Figure 3A and B). The contour plot further demonstrates that thermodynamically unstable siRNAs with the whole ΔG values > -31 kcal/mol tend to stay close to the linear regression line, which also points to the notion that exclusion of thermostable siRNAs makes the correlation coefficient high. Indeed, the correlation coefficient goes higher, when we gradually exclude thermostable siRNAs by elevating the threshold of the whole ΔG values from -52.0 up to -34.6 kcal/mol for *i-Score*, *s-Biopredsi*, *ThermoComposition21* and *DSIR* (Figure 3C). The correlation coefficient, however, goes down when the whole ΔG threshold goes further up, likely because only a limited number of siRNAs can be included in the analysis. Although the whole ΔG values are well correlated

Table 2. Comparison of eight algorithms using subset A831

Threshold	% of effective siRNAs[a]	No (%) of siRNAs matching the threshold	Pearson correlation coefficient
i-Score1600[b,c]			0.592
≥65.9	90	72 (8.8%)	
≥63.0	80	117 (14.1%)	
≥59.4	75	166 (20.0%)	
s-Biopredsi1600[b,c]			0.618
≥0.807	90	73 (8.8%)	
≥0.767	80	141 (17.0%)	
≥0.734	75	197 (23.7%)	
Reynolds[d]			N.D.
≥9	88.9	9 (1.1%)	
≥8	80.4	46 (5.5%)	
≥7	71.0	107 (12.9%)	
Ui-Tei[d]			N.D.
Ia	73.4	64 (7.7%)	
Ia + Ib	68.0	125 (15.0%)	
Amarzguioui[d]			N.D.
≥5	81.0	21 (2.5%)	
≥4	61.3	80 (9.6%)	
≥3	64.8	179 (21.5%)	
Katoh[c]			0.427
≥ 101.1	90	6 (0.7%)	
≥ 87.5	80	31 (3.7%)	
≥79.5	75	80 (11.1%)	
Hsieh			N.D.
=4	50.0	2 (0.2%)	
≥3	51.2	41 (4.9%)	
≥2	52.7	184 (22.1%)	
Takasaki			0.174
n.a.[e]	90	n.a.[e]	
n.a.[e]	80	n.a.[e]	
≥17.1	75	4 (0.5%)	

Note that *i-Score1600*, *s-Boipredsi1600*, *Reynolds* and *Katoh* predict active siRNAs with ~90% accuracy, but the chances of predicting such active siRNAs in a given mRNA with *Reynolds* and *Katoh* are ~1/8 and ~1/12, respectively, of those with *i-Score1600* and *s-BoiPredSi1600*. *ThermoComposition21* and *DSIR* are not included in this analysis, because we cannot avoid overfitting for these two algorithms for subset A831.

[a]Ratios of experimentally proved active siRNAs among siRNAs predicted to be active according to variable thresholds of eight different algorithms. The experimentally proved active siRNAs are arbitrarily defined to those suppressing the gene expression levels to less than 25% of a control.

[b]The *i-Score1600* and *s-Biopredisi1600* scores are different from *i-Score* and *s-Biopredsi*. In order to avoid overfitting for these two algorithms, the modeling algorithms of *i-Score* and *s-Biopredsi* are applied to subset A1600 to calculate scoring parameters for *i-Score1600* and *s-Biopredisi1600*, respectively. The Pearson correlation coefficients between *i-Score* and *i-Score1600*, and *s-Biopredsi* and *s-Biopredsi1600* are 0.990 and 0.985, respectively.

[c]As *i-Score1600*, *s-Biopredsi1600*, *Katoh* and *Takasaki* are continuous numeric scores, thresholds are arbitrarily set so that 90, 80 and 75% siRNAs above the threshold are experimentally proved active. For example, for *i-Score1600*, all the 831 siRNAs in subset A831 are sorted in descending order of *i-Score1600*. The ratio of experimentally proved active siRNAs decreases with decreasing *i-Score1600*. When the lower limit of *i-Score1600* is set to 65.9, 72 siRNAs are included in this category and 65 suppress the gene expression levels to less than 25% of a control. This is how we set an *i-Score1600* threshold for 90% (65/72). The 72 siRNAs comprise 8.8% of the 831 siRNAs in subset A831. This indicates that when we synthesize an siRNA with *i-Score1600* of 65.9 or higher, we can expect that the chance of obtaining an active siRNA is 90%.

[d]For algorithms yielding ordinal or nominal numbers, the indicated ranks are used as the thresholds. For example, for *Reynolds*, the number of siRNAs equal to or higher than the score of 9 is 9, which comprises 1.1% of the 831 siRNAs, and 8 (88.9%) of the 9 siRNAs suppress gene expression levels to less than 25% of a control.

[e]No subgroup of siRNAs matches the criteria of ≥90% or ≥80% prediction accuracy.

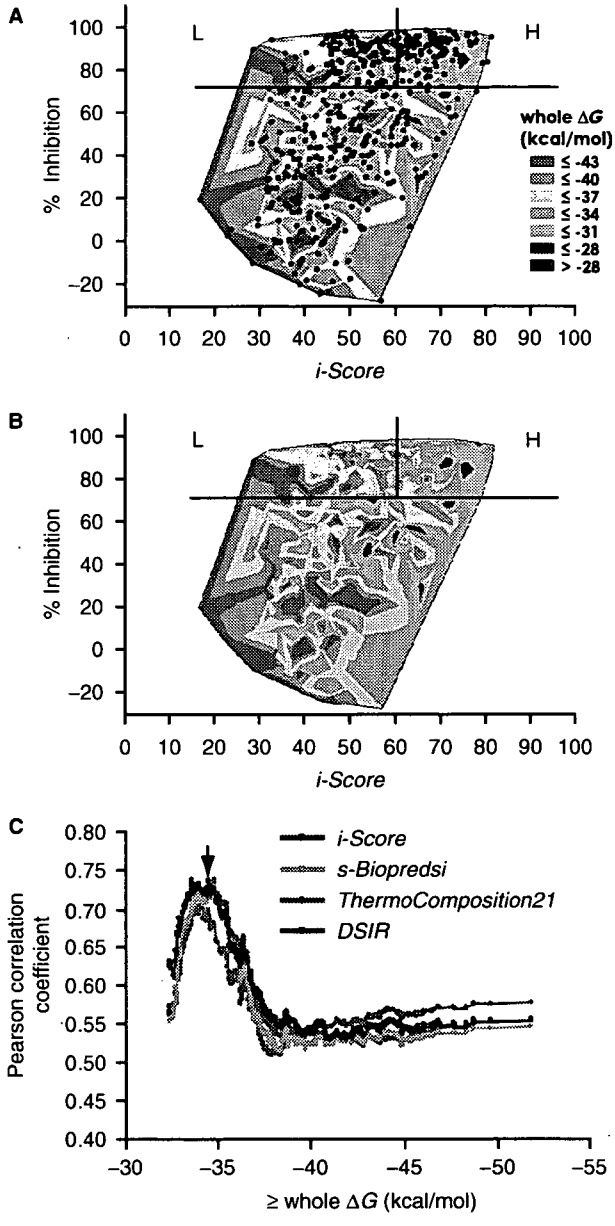

Figure 3. Contours of the whole ΔG values overlaid on the scatted plots of observed and predicted siRNA activities with (**A**) or without (**B**) dots indicating individual siRNAs for dataset B. Area H indicates siRNAs for which *i-Score* successfully predicts siRNA activities, whereas area L indicates siRNAs for which *i-Score* falsely predicts inactive siRNAs. Thermodynamically unstable siRNAs with high whole ΔG values tend to align on a linear regression line (data not shown) going from the bottom left up to the top right, and form a cluster of well-predicted siRNAs (area H) at the top right corner. On the other hand, thermostable siRNAs stay away from the regression line, and form a cluster of poorly predicted siRNAs (area L) at the top left corner. The plots are drawn by the 'contour plot' functionality of the JMP-IN software. (**C**) Correlation coefficients between the observed and predicted siRNA activities in subgroups of siRNAs whose whole ΔG values are equal to or more than the indicated values. For example, there are 101 siRNAs whose whole ΔG values are equal to or more than −34.6 kcal/mol. The correlation coefficient of the 101 siRNAs with *i-Score* is 0.723, and hence 0.723 is plotted on −34.6 (arrow). This is also illustrated in Figure 4. The correlation coefficient tends to go down when the whole ΔG threshold further goes higher, likely because we can include a limited number of siRNAs in the analysis.

with%GC contents ($R = 0.98$), the whole ΔG value is a better discriminator than the%GC content (data not shown).

We found that siRNAs with the whole ΔG value of −34.6 kcal/mol and higher result in a correlation coefficient of 0.723 (Figure 4A), whereas the remaining thermostable siRNAs give rise to a correlation coefficient of 0.514 for dataset B (Figure 4B). ROC analysis also demonstrates that a data subset comprised of unstable siRNAs (≥ -34.6 kcal/mol) gives rise to a markedly higher AUC than that of stable siRNAs (Figure 4C). These analyses all point to the notion that exclusion of thermostable siRNAs improves the correlation between the observed and predicated siRNA activities in all the algorithms.

Genome-wide prediction of active siRNAs with *i-Score*

As shown in Table 2, 90% of siRNAs are active, if we choose siRNAs with *i-Score1600* $\geq$65.9 for subset A831. Additionally, as shown in Figure 4, the whole ΔG value of −34.0 kcal/mol differentiates between successfully and falsely predicted siRNAs. We can thus expect that more than 90% of siRNAs are active, if we set the thresholds of *i-Score* > 66 and the whole ΔG value > −34.0 kcal/mol.

In order to test if *i-Score* can indeed predict active siRNAs in human genes even after we impose a threshold for the whole ΔG value, we applied variable thresholds of *i-Score* and the whole ΔG value to all the transcripts in the NCBI RefSeq Database Build 35.1 (Table 3). When we choose siRNAs with *i-Score* > 65 and the whole ΔG value > −34.0 kcal/mol, we expect to predict 65 active siRNAs per mRNA. Under these conditions, 89.2% of human transcripts are expected to have one or more active siRNAs. These results suggest that *i-Score* potentially predicts active siRNAs in most human genes.

i-Score designer

We developed an Excel VBA program, the *i-Score* designer (Supplementary Data), which calculates 11 different siRNA-designing scores including *i-Score* for all possible siRNA sequences within a gene of our interest or for individually entered siRNA sequences. The program also calculates the whole ΔG value and five other parameters.

A new validation method for siRNA activity

To validate the prediction accuracy of *i-Score*, we developed a universal target vector, pSELL, which accommodates any target sequence in either the sense or antisense direction (Figure 5A). We also constructed the pDual effector vector (30). With pSELL and pDual, a single pair of synthesized oligonucleotides can be inserted into both the target and effector vectors. We constructed 86 pairs of pSELL and pDual vectors (Supplementary Table 4), and assayed their effects in HEK293 cells by measuring the luciferase activities. As expected, *i-Score* predicted siRNA activities more accurately for those with thermodynamically unstable siRNAs (Figure 5B) than those with thermostable siRNAs (Figure 5C).

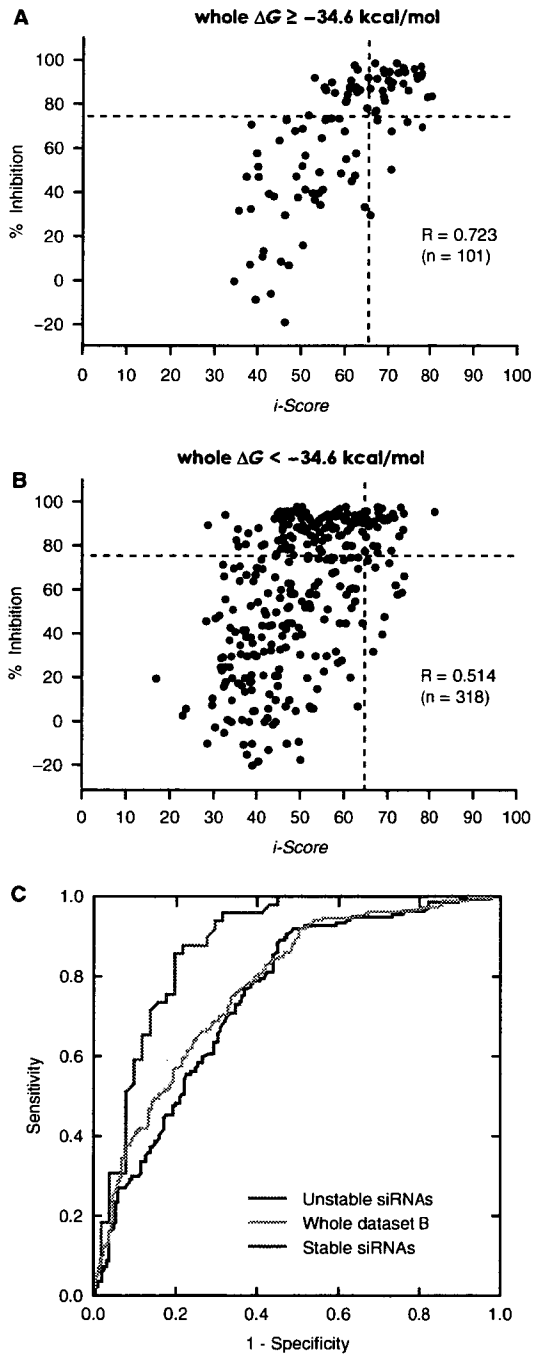

Figure 4. Scattered plots of observed and predicted siRNAs categorized by the whole ΔG values for datasets B. The threshold of whole ΔG values is indicated on top of each panel. *i-Score* predicts activities of thermodynamically unstable siRNAs (**A**) more accurately than those of thermostable siRNAs (**B**). (**C**) ROC curves of thermodynamically unstable (≥ -34.6 kcal/mol) and stable (< -34.6 kcal/mol) siRNAs in dataset B using *i-Score*. AUCs of unstable and stable siRNAs are 0.882 (95% confidence interval, 0.814–0.950) and 0.750 (0.697–0.803), respectively. AUC of the whole dataset B is 0.776 (0.732–0.820).

DISCUSSION

A simple algorithm, *i-Score*, to predict active siRNAs

We developed a simple siRNA-designing algorithm, *i-Score*, by applying a linear regression model to 2431 siRNAs. The correlation coefficient that we achieved with dataset B was as high as those of *s-Biopredsi* (23), *ThermoComposition21* (24,29) and *DSIR* (27). Comparison of *i-Score* with *s-Biopredsi*, as well as with *Reynolds* (8), *Ui-Tei* (9), *Amarzguioui* (11), *Katoh* (33), *Hsieh* (12) and *Takasaki* (10), using subset A831 demonstrated that *i-Score*, *s-Biopredsi*, *Reynolds* and *Katoh* can readily predict active siRNAs with ~90% accuracy. Additionally, both *i-Score* and *s-Biopredsi* predict at least eight times more numbers of active siRNAs than *Reynolds* and *Katoh*. We analyzed the prediction efficiencies under conditions where no overfitting is allowed.

The advantage of *i-Score* over the others is that *i-Score* only takes into account the nucleotide preferences at each position and employs no other parameters, which makes the calculation of *i-Score* simple and easy to trace. In addition, we can visually inspect which nucleotides are better than the others at a specific position. Teramoto and colleagues (34) report that short motifs of 1–3 nt without positional information provide enough parameters for designing siRNAs. Vert and colleagues (27) also report that inclusion of short motifs in addition to the position-specific nucleotide preferences improves the prediction accuracy, and made the *DSIR* scores using a subset of our dataset A. *DSIR* is indeed superior to *i-Score* for dataset A according to our analysis (Table 1). With dataset B, however, prediction accuracy of *DSIR* is not as good as that of *i-Score* (Table 1). This may represent overfittings of *DSIR* with dataset A. Otherwise, either *i-Score* or *DSIR* is applicable to specific datasets but not to the others, but the underlying causes remain elusive.

Exclusion of thermostable siRNAs improves the prediction accuracy

Ladunga (28) reports that the whole ΔG values are correlated with siRNA activities. We also observe a correlation coefficient of $R = 0.279$ between the whole ΔG values and the siRNA activities for dataset A. Inclusion of the whole ΔG value as an independent parameter in our linear regression model, however, fails to improve correlation coefficients for our validation datasets (data not shown). This is likely because the whole ΔG value is already represented in *i-Score*, and indeed the correlation coefficient between these two parameters is 0.445.

We found that exclusion of thermostable siRNAs is beneficial in *i-Score*, *s-Biopredsi*, *ThermoComposition21* and *DSIR* (Figure 3C). We also found that even after we impose a threshold of the whole ΔG values, we can predict enough numbers of active siRNAs for all the human transcripts with *i-Score* (Table 3). Our analysis demonstrates that the whole ΔG value rather serve as a determinant for successful prediction of siRNA activities.

In addition, our analysis demonstrates that some thermostable siRNAs are indeed active (area L in Figure 3A and B), and that no current algorithm can accurately predict their activities. This likely represents the presence of another cluster of siRNAs that potentially

Table 3. Genome-wide prediction of active siRNAs by *i-Score*

i-Score	Whole ΔG	siRNAs/kb[a]	siRNAs/mRNA[b]	Best *i-Score*[c]	10th *i-Score*[d]
>65	–[e]	82.9	132 (99.8%)	82.6 ± 4.3	75.6 ± 4.7
>65	>−34	50.5	65 (95.9%)	82.2 ± 5.3	74.2 ± 7.2
>65	>−30	26.7	33 (89.2%)	81.8 ± 5.9	72.8 ± 7.8
>70	–[e]	34.0	53 (98.8%)	–[f]	–[f]
>70	>−34	24.2	33 (94.0%)	–[f]	–[f]
>70	>−30	14.1	19 (86.9%)	–[f]	–[f]

[a]Average number of active siRNAs per kb of the human RefSeq mRNAs. The NCBI RefSeq Database Build 35.1 includes 40 768 mRNAs, and we analyzed each alternatively spliced transcript as an independent mRNA. The total number of nucleotides that we analyzed is 100 738 984, and the mean and SD of the mRNA length is 2471 ± 2039 bases.
[b]Median number of active siRNAs per mRNA in the human RefSeq database. As the numbers of active siRNAs do not follow a Gaussian distribution, median numbers are represented. The number in parenthesis indicates a percentage of mRNAs among the 40 768 transcripts, harboring at least one siRNA meeting the indicated criteria.
[c]Mean and SD of the highest *i-Score* for each mRNA. mRNAs with no siRNAs above the indicated whole ΔG threshold are excluded from the analysis.
[d]Mean and SD of the 10th highest *i-Score* for each mRNA. mRNAs with less than 10 siRNAs above the indicated whole ΔG threshold are excluded from the analysis.
[e]No threshold is placed for the whole ΔG.
[f]Because means of the best and the 10th highest *i-Scores* are independent of the *i-Score* threshold, values are indicated only on rows of *i-Score* >65.

requires unidentified parameters to precisely predict their activities. Indeed, Krueger and colleagues (35) recently reported that, in addition to the siRNA sequence and its concentration, unidentified characteristics specific to the target gene are likely to have a significant influence on the siRNA activities.

i-Score designer

i-Score predicts on average 65 active siRNAs per mRNA in the genome-wide analysis (Table 3). Other algorithms would also predict similar numbers of active siRNAs. Among these siRNAs, we usually choose a single algorithm and synthesize one or two siRNAs with the best scores. As no algorithm has achieved ~100% prediction accuracy, we usually wonder if the selected siRNAs are indeed active or not. If all the siRNAs, whose scores of an algorithm of our choice are above a predefined threshold, can be analyzed by the other algorithms, the chance of obtaining active siRNAs would become high. Most of the currently available siRNA-designing programs, however, do not provide scores of all available siRNAs within a given gene. To overcome this problem, we implemented 11 different scores and six parameters in *i-Score* designer (Supplementary Data). The *i-Score* designer readily demonstrates how siRNAs selected by an algorithm of our choice are evaluated by the other algorithms. As far as we know, no siRNA-designing program offers such functionality.

pSELL and pDual as a new validation tool of siRNA activity

To validate the prediction accuracy of siRNA-designing algorithms including *i-Score*, we developed a universal target vector, pSELL, in which the target sequence can be inserted in the sense or antisense direction. A combination of the pSELL target vector and the pDual effector vector (30) is cost-effective, because a single pair of oligonucleotides spanning an siRNA sequence of our interest can be inserted into both vectors. Hung and colleagues (36) report a similar cost-effective strategy employing pDual. Their target vector carries a reporter gene of either EGFP or luciferase followed by a target sequence in its 3′ untranslated region. On the other hand, pSELL carries EGFP, the target sequence IRES and the luciferase gene (Figure 5A). First, with pSELL, we can substitute our gene of interest for EGFP, and can quantify the siRNA activity against the full-length mRNA by measuring the expression level of the target mRNA as well as the luciferase activity. Second, pSELL enables us to measure both EGFP and luciferase activities in a single experiment. Third, a unique feature of pSELL is that it accommodates the target sequence in either the sense or antisense direction, which facilitates analysis of an effect of an siRNA on the antisense strand. As a large proportion of mammalian genes harbor antisense transcripts, which regulate the expression levels of the sense transcripts (37), the ability to assay an effect of an siRNA on the antisense strand will become more and more essential when we knock down a gene of our interest.

SUPPLEMENTARY DATA

Supplementary Data are available at NAR Online.

ACKNOWLEDGEMENTS

We appreciate Katsumasa Yamanaka, Akira Ando and Keiko Itano for technical assistance. This work was supported by Grants-in-Aid for COE Research, Scientific Research (A, B and C), Scientific Research on Priority Areas, Exploratory Research from the Ministry of Education, Culture, Sports, Science and Technology of Japan, as well as from the Ministry of Health, Labor and Welfare of Japan, and was also supported in part by grants from the Naito Foundation and the Takeda Science Foundation. Funding to pay the Open Access publication charges for this article was provided by Grants-in-Aid for the Scientific Research on Priority

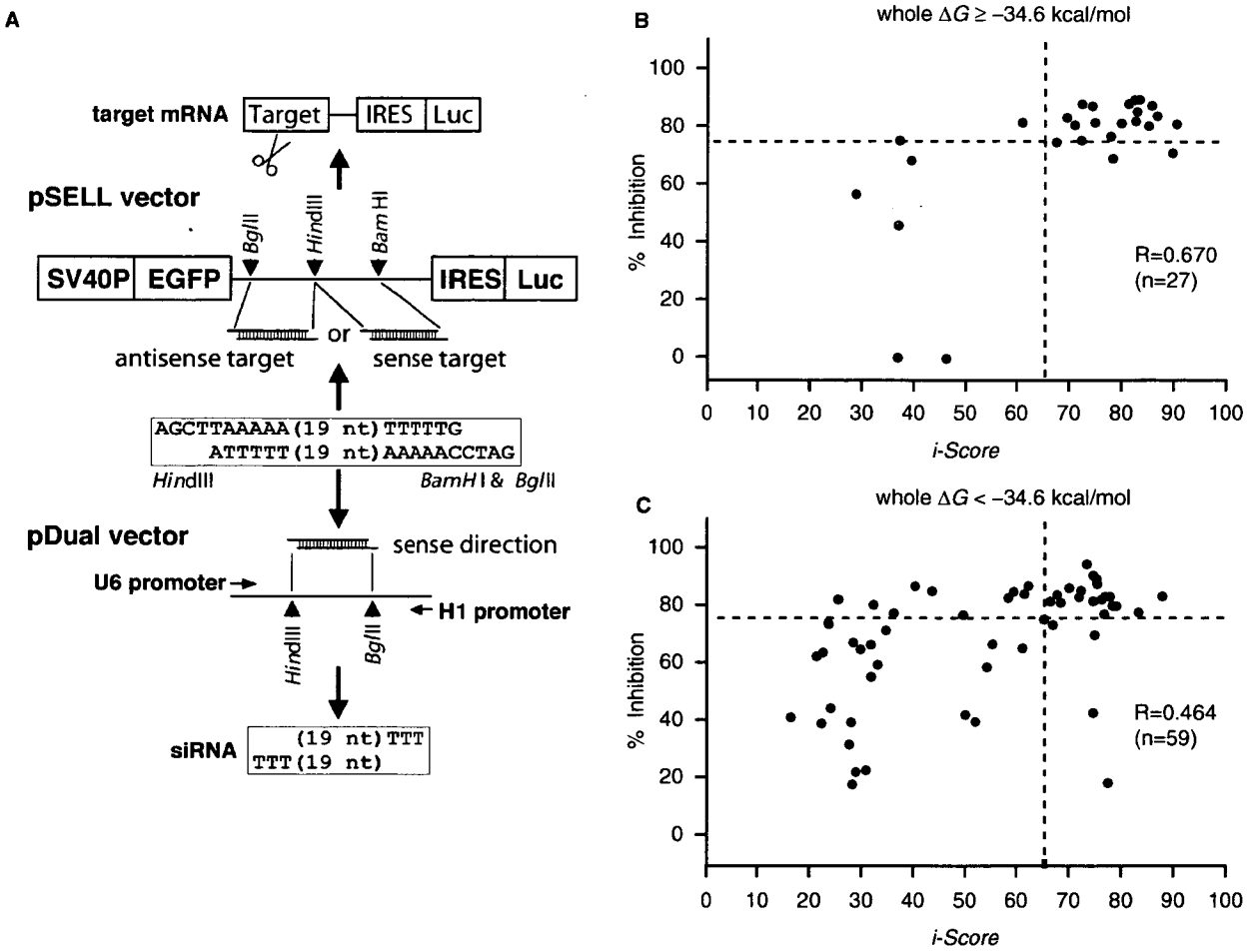

Figure 5. *In vitro* validation of *i-Score* using pSELL and pDual vectors. (**A**) The pSELL target vector carries the SV40 promoter, the *EGFP* gene, the target-cloning site, IRES and the firefly luciferase gene. Synthesized oligonucleotides should carry HindIII- and BamHI/BglII-competent restriction sites at both ends. pSELL can accommodate the synthesized oligonucleotides in either direction. The pDual effector vector harbors the U1 and H1 promoters in opposite directions, and the cloning site between them (30). pDual accommodates the same oligonucleotides as pSELL in the sense direction. siRNA synthesized by pDual works on the target mRNA synthesized by pSELL. We can thus quantify the siRNA activity by measuring the activity of either EGFP or the firefly luciferase. Scattered plots of 86 observed and predicted siRNA activities above (**B**) and below (**C**) the whole ΔG value of −34.6 kcal/mol. The correlation coefficient of thermodynamically unstable siRNAs (**B**) is better than that of thermostable siRNAs (C).

Areas 'System Genomics' from the Ministry of Education, Culture, Sports, Science and Technology of Japan.

Conflict of interest statement. None declared.

REFERENCES

1. McManus,M.T. and Sharp,P.A. (2002) Gene silencing in mammals by small interfering RNAs. *Nat. Rev. Genet.*, **3**, 737–747.
2. Hannon,G.J. (2002) RNA interference. *Nature*, **418**, 244–251.
3. Dorsett,Y. and Tuschl,T. (2004) siRNAs: applications in functional genomics and potential as therapeutics. *Nat. Rev. Drug Discov.*, **3**, 318–329.
4. Dykxhoorn,D.M., Novina,C.D. and Sharp,P.A. (2003) Killing the messenger: short RNAs that silence gene expression. *Nat. Rev. Mol. Cell Biol.*, **4**, 457–467.
5. Kim,D.H. and Rossi,J.J. (2007) Strategies for silencing human disease using RNA interference. *Nat. Rev. Genet.*, **8**, 173–184.
6. Khvorova,A., Reynolds,A. and Jayasena,S.D. (2003) Functional siRNAs and miRNAs exhibit strand bias. *Cell*, **115**, 209–216.
7. Schwarz,D.S., Hutvagner,G., Du,T., Xu,Z., Aronin,N. and Zamore,P.D. (2003) Asymmetry in the assembly of the RNAi enzyme complex. *Cell*, **115**, 199–208.
8. Reynolds,A., Leake,D., Boese,Q., Scaringe,S., Marshall,W.S. and Khvorova,A. (2004) Rational siRNA design for RNA interference. *Nat. Biotechnol.*, **22**, 326–330.
9. Ui-Tei,K., Naito,Y., Takahashi,F., Haraguchi,T., Ohki-Hamazaki,H., Juni,A., Ueda,R. and Saigo,K. (2004) Guidelines for the selection of highly effective siRNA sequences for mammalian and chick RNA interference. *Nucleic Acids Res.*, **32**, 936–948.
10. Takasaki,S., Kotani,S. and Konagaya,A. (2004) An effective method for selecting siRNA target sequences in mammalian cells. *Cell Cycle*, **3**, 790–795.
11. Amarzguioui,M. and Prydz,H. (2004) An algorithm for selection of functional siRNA sequences. *Biochem. Biophys. Res. Commun.*, **316**, 1050–1058.
12. Hsieh,A.C., Bo,R., Manola,J., Vazquez,F., Bare,O., Khvorova,A., Scaringe,S. and Sellers,W.R. (2004) A library of siRNA duplexes targeting the phosphoinositide 3-kinase pathway: determinants of gene silencing for use in cell-based screens. *Nucleic Acids Res.*, **32**, 893–901.
13. Holen,T., Amarzguioui,M., Wiiger,M.T., Babaie,E. and Prydz,H. (2002) Positional effects of short interfering RNAs targeting the human coagulation trigger tissue factor. *Nucleic Acids Res.*, **30**, 1757–1766.

14. Luo,K.Q. and Chang,D.C. (2004) The gene-silencing efficiency of siRNA is strongly dependent on the local structure of mRNA at the targeted region. *Biochem. Biophys. Res. Commun.*, **318**, 303–310.
15. Heale,B.S., Soifer,H.S., Bowers,C. and Rossi,J.J. (2005) siRNA target site secondary structure predictions using local stable substructures. *Nucleic Acids Res.*, **33**, e30.
16. Schubert,S., Grunweller,A., Erdmann,V.A. and Kurreck,J. (2005) Local RNA target structure influences siRNA efficacy: systematic analysis of intentionally designed binding regions. *J. Mol. Biol.*, **348**, 883–893.
17. Saetrom,P. (2004) Predicting the efficacy of short oligonucleotides in antisense and RNAi experiments with boosted genetic programming. *Bioinformatics*, **20**, 3055–3063.
18. Pancoska,P., Moravek,Z. and Moll,U.M. (2004) Efficient RNA interference depends on global context of the target sequence: quantitative analysis of silencing efficiency using Eulerian graph representation of siRNA. *Nucleic Acids Res.*, **32**, 1469–1479.
19. Mittal,V. (2004) Improving the efficiency of RNA interference in mammals. *Nat. Rev. Genet.*, **5**, 355–365.
20. Sandy,P., Ventura,A. and Jacks,T. (2005) Mammalian RNAi: a practical guide. *Biotechniques*, **39**, 215–224.
21. Gong,D. and Ferrell,J.E.Jr. (2004) Picking a winner: new mechanistic insights into the design of effective siRNAs. *Trends Biotechnol.*, **22**, 451–454.
22. Ren,Y., Gong,W., Xu,Q., Zheng,X., Lin,D., Wang,Y. and Li,T. (2006) siRecords: an extensive database of mammalian siRNAs with efficacy ratings. *Bioinformatics*, **22**, 1027–1028.
23. Huesken,D., Lange,J., Mickanin,C., Weiler,J., Asselbergs,F., Warner,J., Meloon,B., Engel,S., Rosenberg,A. *et al.* (2005) Design of a genome-wide siRNA library using an artificial neural network. *Nat. Biotechnol.*, **23**, 995–1001.
24. Shabalina,S.A., Spiridonov,A.N. and Ogurtsov,A.Y. (2006) Computational models with thermodynamic and composition features improve siRNA design. *BMC Bioinformatics*, **7**, 65.
25. Jia,P., Shi,T., Cai,Y. and Li,Y. (2006) Demonstration of two novel methods for predicting functional siRNA efficiency. *BMC Bioinformatics*, **7**, 271.
26. Gong,W., Ren,Y., Xu,Q., Wang,Y., Lin,D., Zhou,H. and Li,T. (2006) Integrated siRNA design based on surveying of features associated with high RNAi effectiveness. *BMC Bioinformatics*, **7**, 516.
27. Vert,J.P., Foveau,N., Lajaunie,C. and Vandenbrouck,Y. (2006) An accurate and interpretable model for siRNA efficacy prediction. *BMC Bioinformatics*, **7**, 520.
28. Ladunga,I. (2007) More complete gene silencing by fewer siRNAs: transparent optimized design and biophysical signature. *Nucleic Acids Res.*, **35**, 433–440.
29. Matveeva,O., Nechipurenko,Y., Rossi,L., Moore,B., Saetrom,P., Ogurtsov,A.Y., Atkins,J.F. and Shabalina,S.A. (2007) Comparison of approaches for rational siRNA design leading to a new efficient and transparent method. *Nucleic Acids Res.*, **35**, e63.
30. Zheng,L., Liu,J., Batalov,S., Zhou,D., Orth,A., Ding,S. and Schultz,P.G. (2004) An approach to genomewide screens of expressed small interfering RNAs in mammalian cells. *Proc. Natl Acad. Sci. USA*, **101**, 135–140.
31. Harborth,J., Elbashir,S.M., Vandenburgh,K., Manninga,H., Scaringe,S.A., Weber,K. and Tuschl,T. (2003) Sequence, chemical, and structural variation of small interfering RNAs and short hairpin RNAs and the effect on mammalian gene silencing. *Antisense Nucleic Acid Drug Dev.*, **13**, 83–105.
32. Vickers,T.A., Koo,S., Bennett,C.F., Crooke,S.T., Dean,N.M. and Baker,B.F. (2003) Efficient reduction of target RNAs by small interfering RNA and RNase H-dependent antisense agents. A comparative analysis. *J. Biol. Chem.*, **278**, 7108–7118.
33. Katoh,T. and Suzuki,T. (2007) Specific residues at every third position of siRNA shape its efficient RNAi activity. *Nucleic Acids Res.*, **35**, e27.
34. Teramoto,R., Aoki,M., Kimura,T. and Kanaoka,M. (2005) Prediction of siRNA functionality using generalized string kernel and support vector machine. *FEBS Lett.*, **579**, 2878–2882.
35. Krueger,U., Bergauer,T., Kaufmann,B., Wolter,I., Pilk,S., Heider-Fabian,M., Kirch,S., Artz-Oppitz,C., Isselhorst,M. *et al.* (2007) Insights into effective RNAi gained from large-scale siRNA validation screening. *Oligonucleotides*, **17**, 237–250.
36. Hung,C.F., Lu,K.C., Cheng,T.L., Wu,R.H., Huang,L.Y., Teng,C.F. and Chang,W.T. (2006) A novel siRNA validation system for functional screening and identification of effective RNAi probes in mammalian cells. *Biochem. Biophys. Res. Commun.*, **346**, 707–720.
37. Katayama,S., Tomaru,Y., Kasukawa,T., Waki,K., Nakanishi,M., Nakamura,M., Nishida,H., Yap,C.C., Suzuki,M. *et al.* (2005) Antisense transcription in the mammalian transcriptome. *Science*, **309**, 1564–1566.
38. Zuker,M. (2003) Mfold web server for nucleic acid folding and hybridization prediction. *Nucleic Acids Res.*, **31**, 3406–3415.

Neurobiology of Disease

CHIP Overexpression Reduces Mutant Androgen Receptor Protein and Ameliorates Phenotypes of the Spinal and Bulbar Muscular Atrophy Transgenic Mouse Model

Hiroaki Adachi,[1] Masahiro Waza,[1] Keisuke Tokui,[1] Masahisa Katsuno,[1,2] Makoto Minamiyama,[1] Fumiaki Tanaka,[1] Manabu Doyu,[1] and Gen Sobue[1]

[1]Department of Neurology, Nagoya University Graduate School of Medicine, Showa-ku, Nagoya 466-8550, Japan, and [2]Institute for Advanced Research, Nagoya University, Showa-ku, Nagoya 466-8550, Japan

Spinal and bulbar muscular atrophy (SBMA) is an inherited motor neuron disease caused by the expansion of a polyglutamine tract within the androgen receptor (AR). The pathologic features of SBMA are motor neuron loss in the spinal cord and brainstem and diffuse nuclear accumulation and nuclear inclusions of the mutant AR in the residual motor neurons and certain visceral organs. Many components of the ubiquitin-proteasome and molecular chaperones are also sequestered in the inclusions, suggesting that they may be actively engaged in an attempt to degrade or refold the mutant AR. C terminus of Hsc70 (heat shock cognate protein 70)-interacting protein (CHIP), a U-box type E3 ubiquitin ligase, has been shown to interact with heat shock protein 90 (Hsp90) or Hsp70 and ubiquitylates unfolded proteins trapped by molecular chaperones and degrades them. Here, we demonstrate that transient overexpression of CHIP in a neuronal cell model reduces the monomeric mutant AR more effectively than it does the wild type, suggesting that the mutant AR is more sensitive to CHIP than is the wild type. High expression of CHIP in an SBMA transgenic mouse model also ameliorated motor symptoms and inhibited neuronal nuclear accumulation of the mutant AR. When CHIP was overexpressed in transgenic SBMA mice, mutant AR was also preferentially degraded over wild-type AR. These findings suggest that CHIP overexpression ameliorates SBMA phenotypes in mice by reducing nuclear-localized mutant AR via enhanced mutant AR degradation. Thus, CHIP overexpression would provide a potential therapeutic avenue for SBMA.

Key words: **CHIP; polyglutamine; SBMA; transgenic mice; protein degradation; androgen receptor**

Introduction

Polyglutamine (polyQ) diseases are inherited neurodegenerative disorders caused by the expansion of trinucleotide CAG repeats in the causative genes (Gatchel and Zoghbi, 2005). To date, nine polyQ diseases have been identified (Di Prospero and Fischbeck, 2005). One of these is spinal and bulbar muscular atrophy (SBMA), characterized by premature muscular exhaustion, progressive muscular weakness, atrophy, and fasciculation in bulbar and limb muscles (Kennedy et al., 1968; Sobue et al., 1993; Sperfeld et al., 2002; Atsuta et al., 2006). In SBMA, a polymorphic CAG repeat with 14–32 CAGs expands to 40–62 CAGs in the first exon of the androgen receptor (*AR*) gene (La Spada et al., 1991; Tanaka et al., 1996). CAG repeat size is inversely correlated with the age at onset and positively correlated with disease severity in SBMA (Doyu et al., 1992; Igarashi et al., 1992; La Spada et al., 1992). The histopathologic hallmarks of SBMA are lower motor neuronal loss (Sobue et al., 1989), diffuse nuclear accumulation, and nuclear inclusions (NIs) of expanded polyQ mutant AR in the residual motor neurons in brainstem and spinal cord as well as in some other visceral organs (Li et al., 1998a,b; Adachi et al., 2005). Such NIs are common pathological features in polyQ diseases and also colocalize with many components of the ubiquitin-proteasome and molecular chaperones (Adachi et al., 2001; Schmidt et al., 2002; Ross and Poirier, 2004), raising the possibility that the ubiquitin-proteasome system and molecular chaperones may actively attempt to degrade or refold components of the inclusions (Stenoien et al., 1999; Ross and Pickart, 2004). Furthermore, these proteasomes and chaperones should also facilitate refolding or proteolysis of toxic misfolded proteins (McClellan et al., 2005) and may play a role in protecting neuronal cells against the toxic properties of expanded polyQ (Cummings et al., 1998; Kobayashi et al., 2000).

C terminus of heat shock cognate protein 70 (Hsc70)-interacting protein (CHIP) has three tetratricopeptide repeat (TPR) domains that interact with the molecular chaperones heat shock protein 70 (Hsp70) and Hsp90 (Ballinger et al., 1999; Connell et al., 2001) and a U-box domain that interacts with the proteasome, conferring CHIP with E3 ubiquitin ligase activity

Received Dec. 25, 2006; accepted April 4, 2007.

This work was supported by a Center of Excellence grant and KAKENHI (17025020) from the Ministry of Education, Culture, Sports, Science, and Technology, Japan; by Special Coordination Funds for Promoting Science and Technology from the Ministry of Education, Culture, Sports, Science, and Technology, Japan; and by grants from the Ministry of Health, Labor, and Welfare, Japan. We have no financial conflict of interest that might be construed to influence the results or interpretation of this manuscript. We thank Jun-ichi Miyazaki for kindly providing the pCAGGS vector and Keiji Tanaka for the pcDNA3-CHIP vector.

Correspondence should be addressed to Dr. Gen Sobue, Department of Neurology, Nagoya University Graduate School of Medicine, 65 Tsurumai-cho Showa-ku, Nagoya 466-8550, Japan. E-mail: sobueg@med.nagoya-u.ac.jp.

DOI:10.1523/JNEUROSCI.1242-07.2007

 0270-6474/07/275115-12$15.00/0

(Hatakeyama et al., 2001; Jiang et al., 2001). Wild-type AR is one of the CHIP substrates (Cardozo et al., 2003; He et al., 2004). CHIP also interacts with misfolded proteins trapped by molecular chaperones and degrades them, thus acting as a "quality control" E3 (Cyr et al., 2002; Murata et al., 2003). In fact, CHIP suppressed inclusion formation and cellular toxicity in cell, zebrafish, and *Drosophila* polyQ disease models (Jana et al., 2005; Miller et al., 2005; Al-Ramahi et al., 2006).

In this study, we examine whether CHIP exerts therapeutic effects on a cultured cell model and a transgenic mouse model expressing the mutant AR to explore a potential strategy for SBMA therapy. We report that CHIP markedly ameliorated motor and pathological phenotypes and that this amelioration was correlated with the reduction of monomeric mutant AR and mutant AR protein complexes in the SBMA models.

Materials and Methods

Cell culture. SH-SY5Y cells were transfected using Lipofectamine 2000 (Invitrogen, Carlsbad, CA) with plasmids encoding ARs containing normal (24 CAGs) or expanded (65 CAGs) polyQ repeats (Waza et al., 2005). Stable clones expressing these normal and mutant ARs were established by selection with the antibiotic G418 (0.4 mg/ml final concentration). The androgen receptor is not expressed in untransfected SH-SY5Y cells. All cell cultures were propagated in the absence of androgen. In Western blots from these cultures, we detected a band of monomeric mutant AR in the separating gel but could hardly detect the high-molecular-weight mutant AR protein complex, which was retained in the stacking gel. Therefore, this cultured cell model is better suited for estimating the change in monomeric mutant AR expression. There was no difference in viability between cells expressing the wild-type and mutant ARs in the absence of androgen using the CellTiter 96 AQueous One Solution Cell Proliferation Assay (Promega, Madison, WI).

DNA transfection. Plasmid pcDNA3-CHIP, encoding FLAG-tagged human CHIP, was kindly provided by Dr. Keiji Tanaka (Laboratory of Frontier Science, Tokyo Metropolitan Institute of Medical Science, Tokyo, Japan) (Murata et al., 2001). AR stable cells were plated in six-well dishes in 2 ml of DMEM/F-12 containing 10% charcoal-stripped fetal bovine serum with penicillin and streptomycin, and each dish was transfected with 4 μg of the vector containing CHIP or mock (negative control) using Lipofectamine 2000 according to the manufacturer's instructions. Transfection efficiency was 60–70%. The cells were cultured for 48 h at 37°C under 5% CO_2.

Transgene construction. Full-length human CHIP cDNA was generated from total RNA extracted from SH-SY5Y cells by reverse transcription-PCR. Full-length human CHIP was constructed by subcloning CHIP inserts derived from the full-length human CHIP cDNA into the pcDNA3.1-myc-his mammalian expression vector (Invitrogen) using PCR. Then, the myc-tagged CHIP fragments were subcloned into the pCAGGS vector (Niwa et al., 1991). All constructs were confirmed by DNA sequence analysis. The final plasmids were digested to remove the transgene.

Generation and maintenance of Tg mice and genotyping. We generated CHIP overexpression mice by microinjection of the transgene into BDF1 fertilized eggs and obtained four founders. BDF1 homozygous CHIP transgenic females were mated with BDF1/B6 male mice expressing full-length human AR with 24 (AR-24Q mice, 5-5 line) or 97-polyQ tracts (AR-97Q mice, 7-8 line), producing a mixed BDF1 and B6 genetic background. First-generation AR-24Q/CHIP$^{(tg/-)}$ or AR-97Q/CHIP$^{(tg/-)}$ mice were mated with either CHIP$^{(tg/-)}$ or CHIP$^{(tg/tg)}$ mice to produce all AR or AR/CHIP double-transgenic mice for each analysis. We screened mouse tail DNA by PCR for the presence of the transgene using the primers 5′-CATCTCAGAAGAGGATCTGTG-3′ and 5′-GGTCGAGGGATCTTCATAAG-3′.

Neurological and behavioral assessment of SBMA model mice. The AR-24Q and AR-97Q mice were generated and maintained as described previously (Katsuno et al., 2002). All animal experiments were performed in accordance with the National Institutes of Health *Guide for the Care and Use of Laboratory Animals* and under the approval of the Nagoya University Animal Experiment Committee. The AR-97Q male mice showed progressive muscular atrophy and weakness as well as diffuse nuclear staining and NIs of the mutant AR. These phenotypes were very pronounced in male transgenic mice, similar to the situation in SBMA patients. The mouse rotarod task (Economex Rotarod; Ugo Basile, Comerio, Italy) was performed on a weekly basis, and cage activity was measured weekly with the AB system (Neuroscience, Tokyo, Japan) as described previously (Katsuno et al., 2002; Minamiyama et al., 2004). Spontaneous motor activity was monitored for 24 h periods; all spontaneous movements, both vertical and horizontal, including locomotion, rearing, and head movements, were counted and automatically totaled.

Immunohistochemistry and histopathology. Mice were deeply anesthetized with ketamine–xylazine and transcardially perfused with 20 ml of 4% paraformaldehyde fixative in phosphate buffer, pH 7.4. Spinal cord and skeletal muscle tissues were removed, postfixed overnight in 10% phosphate-buffered formalin, and processed for paraffin embedding. Sections (6 μm thick) of the above tissues were deparaffinized, dehydrated with alcohol, and treated in formic acid for 5 min at room temperature. For the immunohistochemical studies, the paraffin sections were preheated in a microwave oven for 10 min. The sections were blocked with normal animal serum (1:20) and incubated with mouse anti-expanded polyQ antibody (1:10,000; 1C2; Millipore, Billerica, MA), anti-CHIP antibody (1:1000; Medical and Biological Laboratories, Nagoya, Japan), and mouse anti-glial fibrillary acidic protein (GFAP) antibody (1:1000; Roche Diagnostics, Mannheim, Germany). Primary antibodies were probed with a biotinylated anti-species-specific IgG (Vector Laboratories, Burlingame, CA), and the immune complexes were visualized using streptavidin-horseradish peroxidase (Dako, Glostrup, Denmark) and 3,3′-diaminobenzidine (Dojindo, Kumamoto, Japan) as a substrate. Sections were counterstained with Mayer's hematoxylin. Paraffin-embedded sections (6 μm thick) of the gastrocnemius muscles were air dried and stained with hematoxylin and eosin. For double-immunofluorescence staining of the spinal cord, sections were blocked with 5% normal goat serum and then sequentially incubated with anti-CHIP antibody (1:1000; Medical and Biological Laboratories) and 1C2 antibody (1:10,000; Millipore) at 4°C overnight. The sections were then incubated with Alexa 488-conjugated goat anti-chicken IgG (1:1000; Invitrogen) and Alexa 568-conjugated goat anti-mouse IgG (1:1300; Invitrogen) for 8 h at 4°C. The stained sections were examined and photographed with a confocal laser-scanning microscope (LSM 5 PASCAL; Carl Zeiss MicroImaging, Tokyo, Japan).

Patients. Tissue from nine patients with clinicopathologically and genetically confirmed SBMA (51–84 years of age; mean, 64.3 years), and three non-neurological controls (51–76 years of age; mean, 64.0 years) were also used in the present study. These patients had been hospitalized and followed up at Nagoya University Hospital and its affiliated hospitals during the past 25 years. Informed consent was obtained to use the tissues for research purposes. Paraffin-embedded sections of the spinal cord and brain were obtained and examined in the same way as those from transgenic mice.

Quantification of 1C2-positive cells. For assessment of 1C2-positive cells in the ventral horn of the spinal cord, 50 consecutive transverse sections of the thoracic spinal cord were prepared from each individual mouse, and 1C2-positive cells within the ventral horn of every fifth section were counted as described previously (Adachi et al., 2001). Populations of 1C2-positive cells were expressed as number/mm^2. For assessment of 1C2-positive cells in muscle, the number of 1C2-positive cells was calculated from counts of >500 fibers in randomly selected areas of individual mice and expressed as the number per 100 muscle fibers. The quantitative data of six individual mice were expressed as mean ± SEM.

Protein expression analysis and ubiquitination assay. Forty-eight hours after transfection, cells were lysed in CelLytic-M Mammalian Cell Lysis/Extraction Reagent (Sigma, St. Louis, MO) with 1 mM PMSF and 6 μg/ml aprotinin and centrifuged at 15,000 × *g* for 15 min at 4°C. Sixteen-week-old mice were exsanguinated under ketamine–xylazine anesthesia, and tissues were snap frozen with powdered CO_2 in acetone. The tissues were homogenized in CelLytic-M Mammalian Cell Lysis/Extraction Reagent (Sigma) with 1 mM PMSF and 6 μg/ml aprotinin and centrifuged at

2500 × *g* for 15 min at 4°C. Supernatant fraction protein concentrations were determined using the DC protein assay (Bio-Rad, Hercules, CA). Aliquots of supernatant fractions were loaded on 5–20% SDS-PAGE gels, each lane containing 10 μg of protein for cells, 160 μg for neural tissue, and 80 μg for muscle tissue, and then transferred to Hybond-P membranes (GE Healthcare, Buckinghamshire, UK), using 25 mM Tris, 192 mM glycine, 0.1% SDS, and 10% methanol as transfer buffer. Primary antibodies were used at the following concentrations: rabbit anti-AR, 1:1000 (N20; Santa Cruz Biotechnology, Santa Cruz, CA); rabbit anti-AR, 1:1000 (H280; Santa Cruz Biotechnology); mouse anti-Hsp70, 1:1000 (SPA-810; Stressgen Biotechnologies, San Diego, CA); rabbit anti-Hsp40, 1:5000 (SPA-400; Stressgen Biotechnologies); mouse anti-Hsp90, 1:1000 (F8; Santa Cruz Biotechnology); and mouse anti-α-tubulin, 1:5000 (T9026; Sigma). Primary antibodies were probed using HRP-conjugated anti-rabbit Ig $F(ab')_2$ and anti-mouse Ig $F(ab')_2$ (1:5000; GE Healthcare) secondary antibodies and detected with the ECL Plus kit (GE Healthcare). An LAS-3000 imaging system was used to produce digital images and to quantify band intensities, which were then analyzed with Image Gauge software version 4.22 (Fujifilm, Tokyo, Japan). Densitometric values of AR were normalized to those of endogenous α-tubulin. Relative signal intensity (RSI) was computed as the signal intensity of each sample divided by that of mock-transfected cells (see Fig. 1) or AR-24Q/CHIP$^{(-/-)}$ or AR-97Q/CHIP$^{(-/-)}$ mice (see Fig. 6).

Immunoprecipitation from mouse tissues was performed using 1 mg of total protein lysed in CelLytic-M Mammalian Cell Lysis/Extraction Reagent (Sigma), 15 μl of protein G Sepharose (GE Healthcare) and 2.5 μl of anti-myc antibody (Medical and Biological Laboratories). Protein was eluted from beads by boiling for 5 min in 15 μl of elution buffer (50 mM Tris-HCl, pH 6.8, 2% SDS, 60 μl/ml 2-mercaptoethanol, 10% glycerol) and loaded on SDS-polyacrylamide gels.

For the AR ubiquitination assay, full-length ARs were constructed by subcloning AR inserts derived from pCR-AR24 (24 CAG repeats) or pCR-AR97 (97 CAG repeats) into the pDsRed monomer mammalian expression vector (Takara Bio, Otsu, Japan). SH-SY5Y cells were seeded into 60 mm plates and cotransfected with plasmids encoding DsRed-AR and either CHIP or mock. Cells were exposed to MG132 (5 μM) for a 24 h period. Extracts were prepared, and AR was immunoprecipitated with anti-DsRed antibody. Blots were probed as described for Western blots with ubiquitin antibody (1B3; Medical and Biological Laboratories).

Filter trap assay. To quantify the large-molecular aggregated and soluble forms of the mutant AR protein, filter trap assays of total tissue homogenates from the spinal cord and muscle of male AR-24Q or 97Q mice (16 weeks of age) were performed as described previously (Adachi et al., 2003). Proteins were filtered through a 0.2 μm cellulose acetate membrane (Sartorius, Goettingen, Germany) using a slot-blot apparatus (Bio-Rad). We also put 0.45 μm nitrocellulose membranes (Bio-Rad) under the cellulose acetate membrane to capture the monomeric AR protein passing through this membrane. Only the larger-sized mutant AR protein was retained on the cellulose acetate membrane (pores 0.2 μm in diameter), whereas the nitrocellulose membrane captured protein of all sizes. Samples of protein, 200 μg for spinal cord, and 80 μg for muscle, were prepared in a final volume of 200 μl of lysis buffer, loaded, and gently vacuumed. Slot blots were probed as described for Western blots by an antibody against AR (H-280; Santa Cruz Biotechnology) or α-tubulin (T9026; Sigma).

Pulse-chase labeling assay. Cells were transfected as described above, starved for 1 h in methionine- and cysteine-free DMEM containing 10% dialyzed fetal calf serum, and then labeled for 1 h with 150 μCi of Redivue Pro-Mix L-[^{35}S] *in vitro* cell-labeling mix (GE Healthcare) per milliliter. After washing in PBS, the cells were chased for the indicated time intervals in complete medium. Immunoprecipitation was performed using equivalent amounts of protein lysates, 10 μl of protein G Sepharose (GE Healthcare), and 5 μl of anti-AR antibody (N20; Santa Cruz Biotechnology) as described above. Each sample was separated by 5–20% SDS-PAGE, and analyzed by phosphorimaging (Typhoon 8600 PhosphorImager; GE Healthcare) and Image Gauge software version 4.22 (Fujifilm).

Quantitative real-time reverse transcription-PCR. The levels of AR mRNA were determined by real-time Taqman PCR as described previously (Ishigaki et al., 2002). Total RNA was isolated from SH-SY5Y cells using the RNeasy Mini kit (Qiagen, Valencia, CA) and from transgenic mouse spinal cord and muscle by homogenizing in Trizol (Invitrogen) according to the manufacturer's instructions. Total RNA (5 μg) from cells and mouse spinal cord and muscle were reverse transcribed using SuperScript III reverse transcriptase (Invitrogen). Real-time Taqman reverse transcription (RT)-PCR was performed in a total volume of 50 μl, containing 25 μl of 2× QuantiTect SYBR Green PCR Master Mix (Qiagen) and 10 μM each primer. PCR products were detected by the iCycler system (Bio-Rad). The reaction conditions were 95°C for 15 min and then 45 cycles of 15 s at 94°C, 30 s at 55°C, and 30 s at 72°C. As an internal standard control, the expression level of glyceraldehyde-3-phosphate dehydrogenase (GAPDH) was simultaneously quantified. PCR primers were designed as described previously (Waza et al., 2005). RSI was computed as the signal intensity of each sample divided by that of mock-transfected cells (see Fig. 1*E*) or AR-24Q/CHIP$^{(-/-)}$ or AR-97Q/CHIP$^{(-/-)}$ mice (see Fig. 6*C*).

Statistical analysis. Data were analyzed by unpaired *t* tests in the experiments shown in Figures 1, *B* and *E*, and 6 and log-rank tests for survival rate in that shown in Figure 4*D* using Statview software version 5 (Hulinks, Tokyo, Japan). Statistical significance of the data shown in Figures 1*A*, 4, *A–C* and *F*, and 5*G–H* was examined by the Williams test for multiple comparisons using Microsoft Excel 2004 (Microsoft, Redmond, WA).

Results

Effect of CHIP overexpression on expression and ubiquitination of AR *in vitro*

CHIP directly interacts with and degrades the wild-type AR through its N-terminal conserved motif (He et al., 2004) and induces wild-type AR ubiquitination (Cardozo et al., 2003). To address the question of whether CHIP overexpression promotes the degradation of polyQ-expanded AR, we transfected SH-SY5Y cells stably expressing the wild-type (AR-24Q) or mutant (AR-65Q) AR with varying amounts of CHIP or mock as control. Although immunoblot analysis demonstrated a dose-dependent decline in both wild-type and mutant AR expression after CHIP overexpression (Fig. 1*A*), the monomeric mutant AR decreased significantly more than did the wild type ($p < 0.05$) (Fig. 1*B*), suggesting that the mutant AR is more sensitive to CHIP than is the wild type. CHIP was reported to interact with HSF1 and increase Hsp chaperone levels (Dai et al., 2003; Qian et al., 2006); however, the expression levels of Hsp90, Hsp70, and Hsp40 were not changed after CHIP overexpression (Fig. 1*A*). This finding is consistent with a previous report (Miller et al., 2005) and suggests that the stress-induced response is different among different cell types.

To determine whether the enhanced degradation of mutant AR was attributable to protein degradation or to changes in RNA expression, the turnover of wild-type and mutant AR was then assessed with a pulse-chase labeling assay. SH-SY5Y stable cells were transiently transfected with mock or CHIP constructs. Without CHIP, the wild-type and mutant ARs were degraded almost equally, as reported previously (Bailey et al., 2002; Lieberman et al., 2002). In the presence of overexpressed CHIP, however, the wild-type and mutant ARs had half-lives of 3.6 and 2.7 h, respectively (Fig. 1*D*), whereas mRNA levels for both the wild-type and mutant AR were quite similar (Fig. 1*E*). These data indicate that CHIP preferentially degrades the mutant AR protein without altering mRNA levels.

The preferential degradation of mutant AR by CHIP suggests that CHIP may promote mutant AR ubiquitination, thereby targeting it for degradation. To assess this possibility, SH-SY5Y cells were transiently cotransfected with CHIP and DsRed-tagged AR-24Q or AR-97Q, and the cell lysates were immunoprecipitated with anti-DsRed. In this experiment, blots were probed with anti-

ubiquitin antibody. No ubiquitination was detected in control cells without expression of AR. Although both AR-24Q and AR-97Q were ubiquitinated without coexpression of CHIP, AR-97Q was more strongly ubiquitinated. The levels of ubiquitinated AR were further increased in cells simultaneously expressing mutant AR and CHIP (Fig. 1*F*). CHIP expression significantly enhanced the level of ubiquitinated mutant AR but only slightly enhanced that of the wild-type AR (Fig. 1*F*).

Colocalization of CHIP with mutant AR in the nuclei

Next, we evaluated the colocalization of endogenous CHIP and mutant AR in AR-97Q mice and in SBMA patients. Double-immunofluorescence staining with chicken anti-CHIP and mouse anti-expanded polyQ (1C2) antibodies revealed that the endogenous CHIP (Fig. 2*A*,*D*,*G*,*J*) and mutant AR (Fig. 2*B*,*E*,*H*,*K*) were colocalized diffusely in the nuclei (Fig. 2*C*,*I*) and NIs (Fig. 2*F*,*L*) in the spinal anterior horn neurons of the AR-97Q mice and in the hypoglossal nucleus cells and spinal anterior horn neurons of SBMA patients, suggesting that the endogenous CHIP coexists with mutant AR and exerts its function in both AR-97Q mice and SBMA patients.

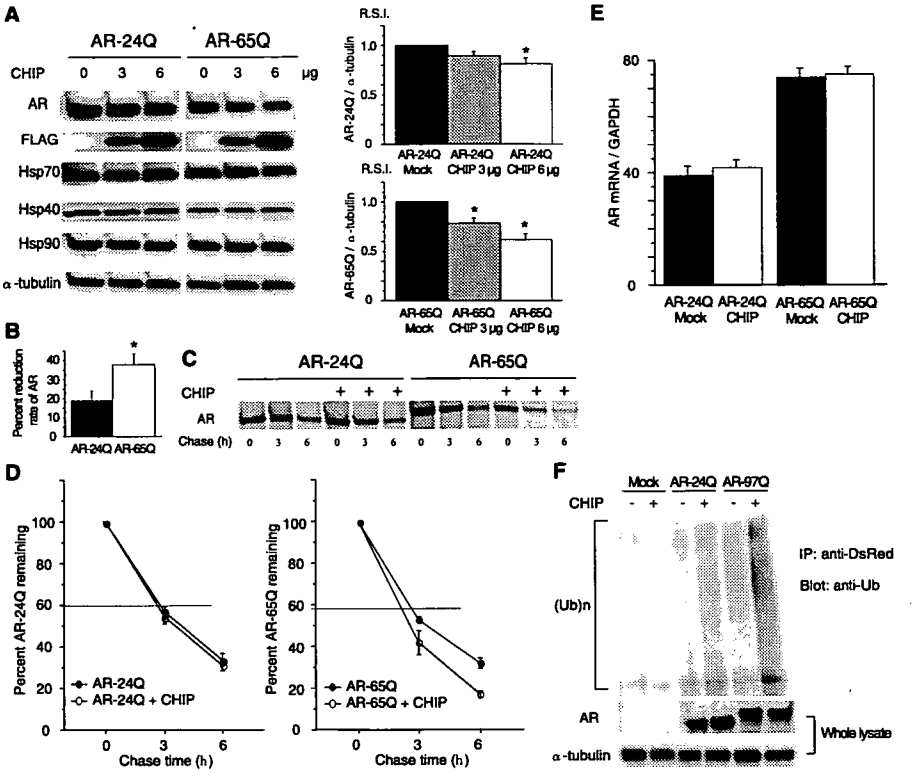

Figure 1. Effect of CHIP on the AR or chaperones in cultured cells. ***A***, Although anti-AR (N20) immunoblotting and densitometry demonstrated a dose-dependent decline of both wild-type (24Q) and mutant (65Q) AR expression in response to CHIP overexpression, the mutant AR decreased more than did the wild type. Mean levels of AR-24Q and AR-65Q expression were relatively compared between CHIP-transfected cells and mock-transfected cells. CHIP overexpression did not increase the expression of Hsp70, Hsp40, and Hsp90. $*p < 0.005$. ***B***, The decrease in mutant AR in response to CHIP overexpression was much higher than that of the wild type (18.8% vs 38.0%; 6 μg of CHIP). $*p < 0.05$. ***C***, Pulse-chase analysis of two forms of AR. Data are from one representative experiment for wild-type and mutant AR. ***D***, Pulse-chase assessment of the half-life of wild-type (left) and mutant (right) AR. The percentages of AR-24Q and AR-65Q remaining in the absence (●) and presence (○) of overexpressed CHIP are indicated. Mutant AR was degraded more rapidly than the wild-type AR in the presence of overexpressed CHIP. ***E***, Real-time RT-PCR of wild-type and mutant AR mRNA normalized to GAPDH levels. The wild-type and mutant AR mRNA levels were similar under CHIP overexpression. ***F***, Ubiquitination of AR in control, AR-24Q-, and AR-97Q-transfected cells in the absence (−) or presence (+) of CHIP cotransfection. No ubiquitination was detected in control cells without expression of AR. Although both AR-24Q and AR-97Q were ubiquitinated without coexpression of CHIP, AR-97Q was strongly ubiquitinated. CHIP significantly enhanced the level of mutant AR ubiquitination but only slightly enhanced that of wild-type AR. ***A***, ***B***, ***D***, ***E***, Values represent means ± SEM ($n = 5$). IP, Immunoprecipitation; Ub, ubiquitin.

Nondeleterious effects of CHIP overexpression and generation of double-transgenic mice

Because CHIP colocalizes with polyQ-expanded AR, we further tested the effects of CHIP overexpression in the SBMA transgenic mouse model to explore a potential strategy for SBMA therapy. We generated transgenic mice expressing full-length human CHIP under the control of a cytomegalovirus enhancer and a chicken β-actin promoter (Fig. 3*A*). From 14 available lines, we established four that express CHIP in the brain and skeletal muscle and examined the effects of overexpressed CHIP on mouse phenotypes. Through 50 weeks of age, none of the hemizygous or homozygous transgenic mice overexpressing CHIP showed any neurological phenotypes assessed using the rotarod task; they did, however, display slightly delayed weaning. Histological examination at 50 weeks did not show any detectable effects on neuronal cell morphology, neuronal cell number, or muscle structure (data not shown). These studies indicated that overexpression of human CHIP alone does not impair neuronal development or motor function.

To determine whether overexpression of human CHIP could ameliorate the disease phenotype of the SBMA transgenic mouse model, we crossed the AR-24Q mice and the AR-97Q mice (Katsuno et al., 2002) with mice overexpressing human CHIP (CHIP2 line). The AR-97Q mice (SBMA model) are small and have short lifespans, progressive muscle atrophy, and weakness, as well as reduced cage activity (Katsuno et al., 2002). Because these phenotypes are markedly pronounced in the males, similar to SBMA patients (Katsuno et al., 2002), we used male transgenic mice in this study. We generated AR-24Q/CHIP$^{(tg/tg)}$ and AR-97Q/CHIP$^{(tg/tg)}$ mice as homozygotes, the AR-24Q/CHIP$^{(tg/-)}$ and AR-97Q/CHIP$^{(tg/-)}$ mice as hemizygotes, and the AR-24Q/CHIP$^{(-/-)}$ and AR-97Q/CHIP$^{(-/-)}$ mice as controls. The AR transgene expression was at the hemizygous level in all AR-24Q/CHIP and AR-97Q/CHIP double transgenics.

Expression of CHIP in double-transgenic mice

We examined whether the AR/CHIP double-transgenic mice express increased levels of the CHIP protein in the spinal cord and skeletal muscle. Western blot analysis revealed that CHIP expression in the spinal cords of AR-97Q/CHIP$^{(tg/-)}$ and AR-97Q/CHIP$^{(tg/tg)}$ mice was three and six times as high, respectively, as endogenous CHIP in the AR-97Q/CHIP$^{(-/-)}$ mice. In muscle, it was six times as high in the AR-97Q/CHIP$^{(tg/-)}$ mice and 12 times as high in the AR-97Q/CHIP$^{(tg/tg)}$ mice (Fig. 3*B*). As in transfected cells, the expression levels of Hsp90, Hsp70, and Hsp40 were not changed after CHIP overexpression in the double-transgenic mice (Fig. 3*B*). The increased CHIP was coim-

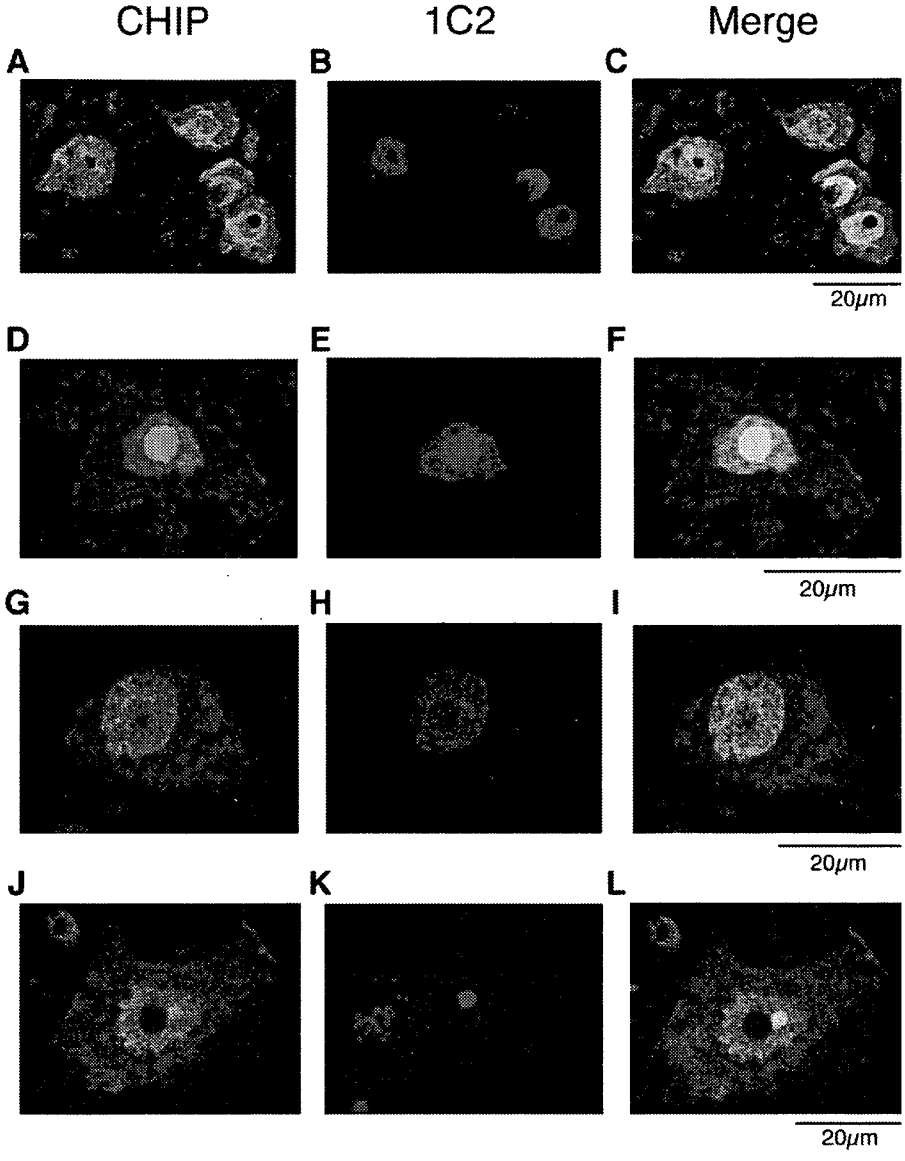

Figure 2. Colocalization of nuclear-localized CHIP with mutant AR. ***A–L***, Anti-CHIP and anti-polyQ immunohistochemistry in spinal cords of 16-week-old AR-97Q mice (***A–F***) and an SBMA patient (***G–L***). ***A–C***, Double-immunofluorescence staining for CHIP (***A***; green), expanded-polyQ (***B***; red), and overlay of the two signals (***C***; yellow) in the spinal anterior horn cells. ***D–F***, CHIP (green; ***D***) and mutant AR (red; ***E***) are colocalized in nuclear inclusions (shown in yellow; ***F***) in the spinal anterior horn cell. ***G–I***, Double-immunofluorescence staining in cells of the hypoglossal nucleus of an SBMA patient revealed diffuse nuclear colocalization of CHIP (***G***) and mutant AR (***H***, ***I***). ***J–L***, CHIP (green; ***J***) and mutant AR (red; ***K***) were also colocalized in NIs (shown in yellow; ***L***) in the spinal anterior horn cell of SBMA patients.

munoprecipitated with polyQ-expanded AR and Hsp70, suggesting that CHIP may recognize AR either directly or indirectly through association with Hsp70 (Fig. 3*C*). We also performed Western blotting analysis using 8-, 16-, 24-, and 32-week-old CHIP$^{(tg/tg)}$ and AR-97Q/CHIP$^{(tg/tg)}$ mice to examine the effect of age on the expression level of CHIP in spinal cord and muscle. We found that the expression levels of CHIP did not change even in the 32-week-old mice (Fig. 3*D*). Immunohistochemical studies of double-transgenic mice tissue stained with the CHIP-specific antibody confirmed that spinal anterior horn neurons and muscle cells expressed the CHIP (Fig. 3*E*,*F*). CHIP protein was diffusely distributed in the nuclei and cytoplasm (Fig. 3*E*,*F*). Glial cells also showed diffuse nuclear staining of CHIP protein (Fig. 3*E*).

Human CHIP overexpression ameliorates phenotypic expression of SBMA mice

To determine whether CHIP overexpression has an ameliorative effect on the motor phenotypes in the double-transgenic mice, we performed the rotarod task and measured locomotor cage activity with an infrared sensor system (Fig. 4*A*,*B*). Motor impairment on the rotarod task was evident in the AR-97Q/CHIP$^{(-/-)}$ mice as early as 8 weeks after birth but was seen, to a lesser degree, in the AR-97Q/CHIP$^{(tg/tg)}$ mice beginning at only 16 weeks (Fig. 4*A*). Although both the AR-97Q/CHIP$^{(tg/tg)}$ and AR-97Q/CHIP$^{(tg/-)}$ mice performed significantly better than the AR-97Q/CHIP$^{(-/-)}$ mice ($p < 0.005$ and $p < 0.025$, respectively) (Fig. 4*A*), the AR-97Q/CHIP$^{(tg/tg)}$ mice were on the rod longer than the AR-97Q/CHIP$^{(tg/-)}$ mice during the trial. The locomotor cage activity of the AR-97Q/CHIP$^{(-/-)}$ mice was also significantly decreased at 32 weeks compared with the other two double transgenics ($p < 0.005$, respectively) (Fig. 4*B*). Although there were no differences in body weight at birth among the various lines, the AR-97Q/CHIP$^{(-/-)}$ mice lost weight significantly earlier than did the AR-97Q/CHIP$^{(tg/-)}$ and AR-97Q/CHIP$^{(tg/tg)}$ mice ($p < 0.005$) (Fig. 4*C*). The survival rate was significantly higher in the AR-97Q/CHIP$^{(tg/-)}$ and AR-97Q/CHIP$^{(tg/tg)}$ mice than in the AR-97Q/CHIP$^{(-/-)}$ mice ($p < 0.0001$) (Fig. 4*D*). Because the decrease in ameliorative effects of CHIP overexpression in the aged mice is not attributable to decreased CHIP expression (Fig. 3*D*), it is probably caused by the progressive nuclear accumulation of toxic mutant AR in the aged mice (Katsuno et al., 2003). The affected AR-97Q/CHIP$^{(-/-)}$ mice exhibited motor weakness, took short steps, or dragged their legs, whereas the AR-97Q/CHIP$^{(tg/tg)}$ mice moved almost normally, and the AR-97Q/CHIP$^{(tg/-)}$ mice only took somewhat shorter steps (Fig. 4*E*). Both the AR-97Q/CHIP$^{(tg/-)}$ and AR-97Q/CHIP$^{(tg/tg)}$ mice took significantly longer steps than the AR-97Q/CHIP$^{(-/-)}$ mice ($p < 0.005$) (Fig. 4*F*). Although the SBMA phenotypes were ameliorated in both the AR-97Q/CHIP$^{(tg/tg)}$ and AR-97Q/CHIP$^{(tg/-)}$ mice, the AR-97Q/CHIP$^{(tg/tg)}$ mice were better than the AR-97Q/CHIP$^{(tg/-)}$ mice in most of the parameters, suggesting that the improved motor phenotype depended on the CHIP expression level rather than the genetic background.

Immunohistochemical staining for mutant AR using the 1C2 antibody showed a marked reduction in diffuse nuclear staining and NIs in spinal cord (Fig. 5*A–C*) and muscle (Fig. 5*D–F*) of the AR-97Q/CHIP$^{(tg/-)}$ and AR-97Q/CHIP$^{(tg/tg)}$ mice compared with the AR-97Q/CHIP$^{(-/-)}$ mice. In the AR-97Q/CHIP$^{(-/-)}$ mice, intense staining was frequently seen in the nuclei (Fig.

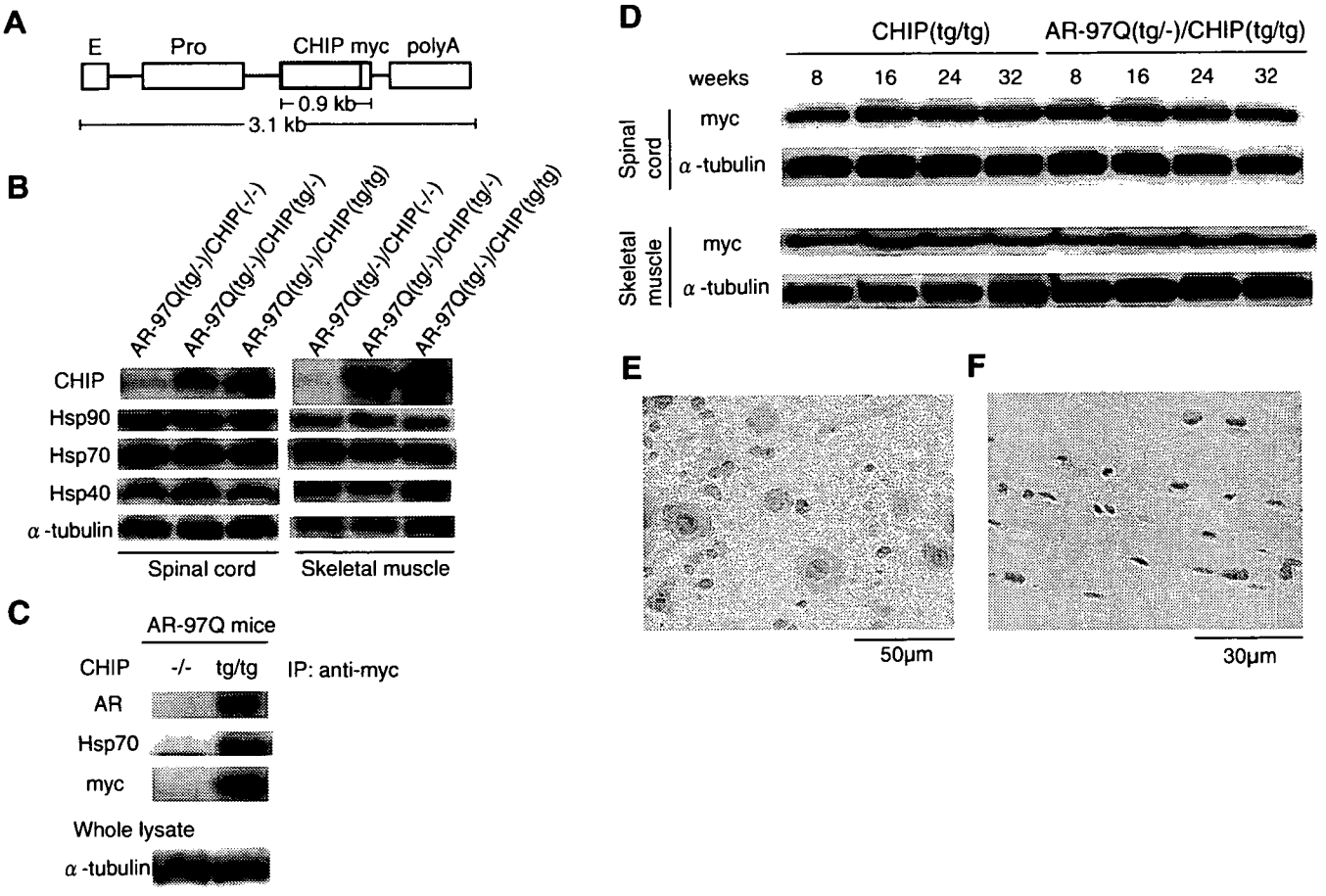

Figure 3. Increased CHIP expression in double-transgenic mice. ***A***, Schematic view of the transgene construct. The microinjected fragment was composed of a cytomegalovirus enhancer (E), a chicken β-actin promoter (Pro), full-length human CHIP with a myc tag, and a rabbit β-globin polyadenylation signal sequence (polyA). ***B***, Western blot analysis of total spinal cord and muscle protein lysates from AR-97Q/CHIP$^{(-/-)}$, AR-97Q/CHIP$^{(tg/-)}$, and AR-97Q/CHIP$^{(tg/tg)}$ mice immunolabeled with antibodies against CHIP, Hsp90, Hsp70, and Hsp40. ***C***, Coimmunoprecipitation Western blots for CHIP. Soluble fractions were collected from the spinal cord of AR-97Q/CHIP$^{(-/-)}$ and AR-97Q/CHIP$^{(tg/tg)}$ mice. Equal amounts of protein were immunoprecipitated with an antibody to myc and immunoblotted for AR and Hsp70. Coimmunoprecipitation of CHIP and the polyQ-expanded mutant AR or the Hsp70 chaperone was detected. ***D***, Western blot analysis of CHIP expression in total spinal cord and muscle protein lysates from CHIP$^{(tg/tg)}$ and AR-97Q/CHIP$^{(tg/tg)}$ mice of the indicated ages, immunolabeled with antibodies against myc. ***E***, ***F***, CHIP immunohistochemistry in spinal anterior horn and skeletal muscle of 16-week-old AR-97Q/CHIP$^{(tg/tg)}$ mice counterstained with Mayer's hematoxylin. ***E***, CHIP immunoreactivity is localized to the nuclei and cytoplasm, with intense and diffuse staining in the anterior horn cells. ***F***, Skeletal muscle showed diffuse nuclear and cytoplasmic staining. IP, Immunoprecipitation.

5*A*,*D*), whereas staining was infrequent in the AR-97Q/CHIP$^{(tg/-)}$ mice (Fig. 5*B*,*E*) and much less frequent in the AR-97Q/CHIP$^{(tg/tg)}$ mice (Fig. 5*C*,*F*). There were significantly more 1C2-positive cells in spinal cord (Fig. 5*G*) and muscle (Fig. 5*H*) of the AR-97Q/CHIP$^{(-/-)}$ mice than in the AR-97Q/CHIP$^{(tg/-)}$ and AR-97Q/CHIP$^{(tg/tg)}$ mice. The 1C2-positive cell populations were not, however, statistically different in the AR-97Q/CHIP$^{(tg/-)}$ and AR-97Q/CHIP$^{(tg/tg)}$ mice. GFAP-specific antibody staining showed an apparent reduction in reactive astrogliosis in the AR-97Q/CHIP$^{(tg/tg)}$ mice compared with the AR-97Q/CHIP$^{(-/-)}$ mice in the spinal anterior horn (Fig. 5*I*). Muscle histology also demonstrated marked amelioration of muscle atrophy in the AR-97Q/CHIP$^{(tg/tg)}$ mice (Fig. 5*J*). The AR-24Q/CHIP mice displayed no altered phenotypes (data not shown). The numbers of neuronal cells in the spinal ventral horns of AR-97Q/CHIP$^{(-/-)}$, AR-97Q/CHIP$^{(tg/-)}$, and AR-97Q/CHIP$^{(tg/tg)}$ mice were not significantly decreased compared with those in the wild-type mice (data not shown).

Overexpression of CHIP decreases the high-molecular-weight mutant AR protein and monomeric mutant AR protein

Because the mutant AR was preferentially degraded compared with the wild-type AR when CHIP was overexpressed *in vitro*, we also examined levels of AR in the SBMA mouse model. Western blot analysis from lysates of the spinal cord and muscle of AR-97Q mice revealed high-molecular-weight mutant AR protein complex retained in the stacking gel as well as a band of monomeric mutant AR, whereas only the band of wild-type monomeric AR was visible in tissues from the AR-24Q mice (Fig. 6*A*,*B*). CHIP overexpression notably diminished both the high-molecular-weight complex and the monomer of mutant AR in the spinal cord and muscle of the AR-97Q mice but only slightly diminished the wild-type monomeric AR in AR-24Q mice (Fig. 6*A*,*B*). CHIP overexpression decreased the amount of the monomeric AR in AR-97Q mice by 50% in the spinal cord and 75% in the skeletal muscle but only by 8% and 5%, respectively, in AR-24Q mice (Fig. 6*A*,*B*). The levels of wild-type and mutant AR mRNA were similar in both AR-24Q and AR-97Q mice under CHIP overexpression (Fig. 6*C*). These observations suggest that overexpression of CHIP markedly decreases not only the monomeric mutant AR protein but also the high-molecular-weight mutant AR protein.

We also performed filter trap assays to quantitatively analyze the effects of CHIP overexpression on levels of both the large-molecular aggregated and soluble forms of mutant AR (Wanker et al., 1999). Only the larger-sized mutant AR protein was re-

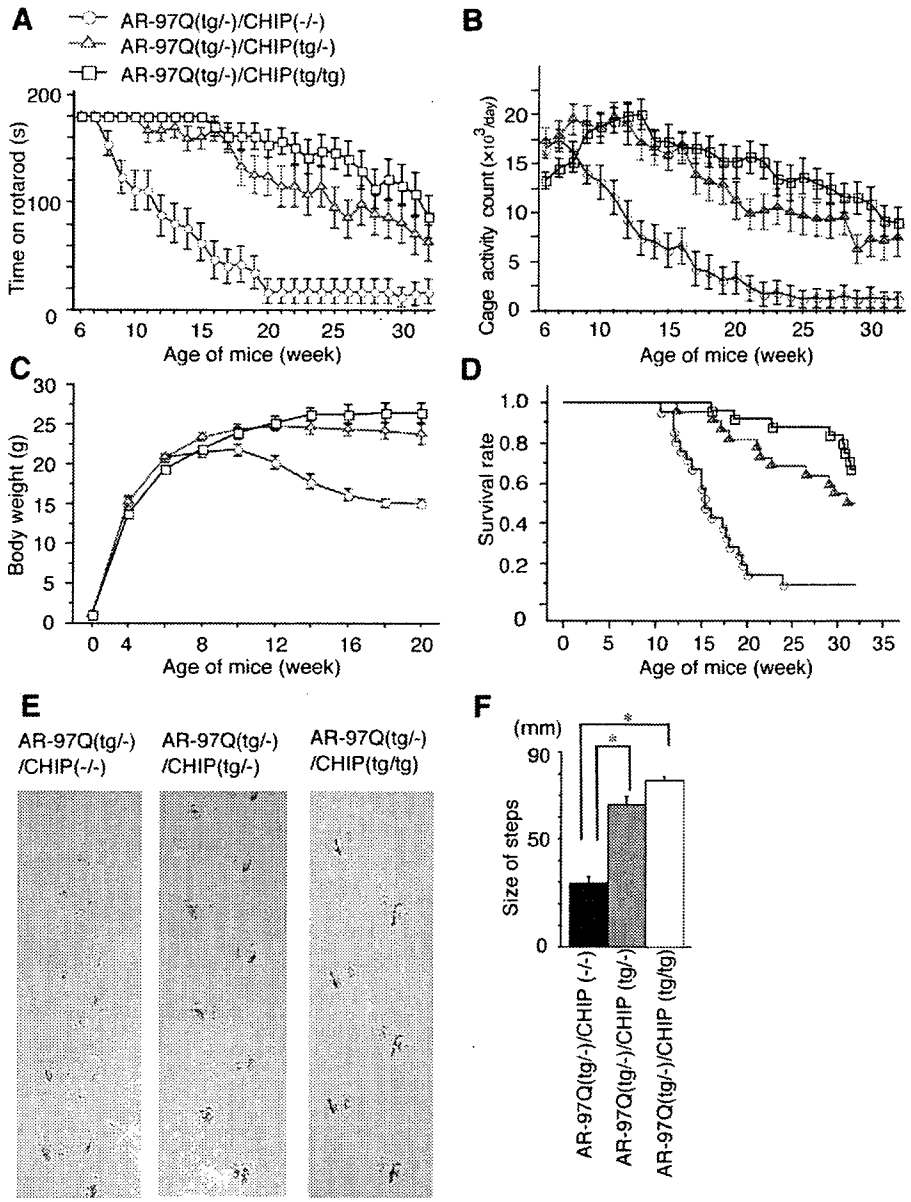

Figure 4. Effects of human CHIP overexpression on the behavioral phenotypes in male AR-97Q mice. ***A–D***, Rotarod task (***A***; $n = 22$), cage activity (***B***; $n = 22$), body weight (***C***; $n = 26$), survival rate (***D***; $n = 26$) of the AR-97Q/CHIP$^{(-/-)}$ (○), AR-97Q/CHIP$^{(tg/-)}$ (□), and AR-97Q/CHIP$^{(tg/tg)}$ mice (△). AR-97Q mice overexpressing human CHIP remained longer on the rotarod and showed higher cage activity than the AR-97Q/CHIP$^{(-/-)}$. The AR-97Q/CHIP$^{(-/-)}$ lost weight earlier than the other two double transgenics. ***D***, A Kaplan-Meier plot shows the prolonged survival of AR-97Q/CHIP$^{(tg/-)}$ and AR-97Q/CHIP$^{(tg/tg)}$ mice compared with the AR-97Q/CHIP$^{(-/-)}$. The AR-97Q/CHIP$^{(-/-)}$ mice were significantly different from either of the other two in all parameters tested. Moreover, the AR-97Q/CHIP$^{(tg/-)}$ mice were worse off than the AR-97Q/CHIP$^{(tg/tg)}$ in all parameters tested. ***E***, Footprints of representative 16-week-old AR-97Q/CHIP$^{(-/-)}$, AR-97Q/CHIP$^{(tg/-)}$, and AR-97Q/CHIP$^{(tg/tg)}$ mice. Front paws are indicated in red, and hindpaws are indicated in blue. AR-97Q/CHIP$^{(-/-)}$ mice exhibit motor weakness with dragging of the legs, AR-97Q/CHIP$^{(tg/tg)}$ mice walk almost normally, and AR-97Q/CHIP$^{(tg/-)}$ mice walk with somewhat shorter steps. ***F***, The average length of hindpaw steps in 16-week-old AR-97Q/CHIP$^{(-/-)}$, AR-97Q/CHIP$^{(tg/-)}$, and AR-97Q/CHIP$^{(tg/tg)}$ mice. Values are expressed as means ± SEM ($n = 6$). *$p < 0.005$.

tained on the upper, cellulose acetate membrane (pores 0.2 μm in diameter), whereas the lower nitrocellulose membrane captured all proteins that passed through the upper membrane (Fig. 6*D*). Values were normalized to endogenous α-tubulin trapped on the nitrocellulose membrane. Both forms of trapped AR-97Q protein were markedly reduced in the spinal cord and muscle of mice overexpressing CHIP, whereas levels of soluble monomeric AR protein from the AR-24Q mice were only slightly reduced (Fig. 6*D*). The endogenous AR protein was not retained on the cellulose acetate membrane in wild-type mice (data not shown). These results strongly indicate that CHIP markedly reduces not only the monomeric mutant AR protein but also the high-molecular-weight mutant AR complex, by preferentially degrading the mutant AR. These observations also suggest that overexpression of CHIP enhanced the function of the ubiquitin-proteasome pathway and subsequently accelerated degradation of monomeric mutant AR protein.

Discussion

CHIP is a U-box-dependent E3 ubiquitin ligase that associates with the Hsp70 and Hsp90 molecular chaperones and targets folded or toxic misfolded proteins for degradation (McDonough and Patterson, 2003). A wide range of different proteins have been identified as CHIP substrates, including members of the steroid hormone receptor family (Connell et al., 2001; Tateishi et al., 2004; Wang and DeFranco, 2005), the cystic-fibrosis transmembrane-conductance regulator (Meacham et al., 2001; Younger et al., 2006), E2A transcription factors (Huang et al., 2004), raf-1 protein kinase (Demand et al., 2001), ErbB2 (Zhou et al., 2003), nucleophosmin-anaplastic lymphoma kinase (Bonvini et al., 2004), dual leucine zipper-bearing kinase (Daviau et al., 2006), caytaxin (Grelle et al., 2006), αB-crystallin (Chavez Zobel et al., 2003), tau (Hatakeyama et al., 2004; Petrucelli et al., 2004; Sahara et al., 2005; Dickey et al., 2006), α-synuclein (Shin et al., 2005), the p53 tumor suppressor (Esser et al., 2005), apoptosis signal-regulating kinase 1 (Hwang et al., 2005), and polyQ-disease causative proteins (Jana et al., 2005; Miller et al., 2005; Al-Ramahi et al., 2006). CHIP can directly interact with and degrade the wild-type AR in a phosphorylation-dependent or -independent manner (Cardozo et al., 2003; Rees et al., 2006) and can repress AR transcriptional activity, suggesting that CHIP may play a role in regulating AR function in the cell (He et al., 2004). CHIP also has been shown to associate with the polyQ-expanded AR (Thomas et al., 2004). In this study, we addressed the question of whether CHIP overexpression promotes the degradation of mutant AR and exerts therapeutic effects on the SBMA phenotype. In a cultured neuronal cell model of SBMA, we demonstrated that increasing levels of CHIP more effectively ubiquitinated and degraded the monomeric mutant AR than the wild-type AR, suggesting that the mutant AR is more sensitive to CHIP than is the wild type. Overexpression of CHIP strongly inhibited nuclear accumulation of the mutant AR and markedly ameliorated motor impairments in SBMA transgenic mice in a dose-dependent manner. Mutant AR and CHIP were co-localized diffusely in the nuclei and in the NIs in neurons of the